

---


Electronic Theses and Dissertations, 2004-2019

---

2009

## Classical Size Effect In Copper Thin Films: Impact Of Surface And Grain Boundary Scattering On Resistivity

Tik Sun  
*University of Central Florida*

 Part of the [Materials Science and Engineering Commons](#)  
Find similar works at: <https://stars.library.ucf.edu/etd>  
University of Central Florida Libraries <http://library.ucf.edu>

This Doctoral Dissertation (Open Access) is brought to you for free and open access by STARS. It has been accepted for inclusion in Electronic Theses and Dissertations, 2004-2019 by an authorized administrator of STARS. For more information, please contact [STARS@ucf.edu](mailto:STARS@ucf.edu).

---

### STARS Citation

Sun, Tik, "Classical Size Effect In Copper Thin Films: Impact Of Surface And Grain Boundary Scattering On Resistivity" (2009). *Electronic Theses and Dissertations, 2004-2019*. 3927.  
<https://stars.library.ucf.edu/etd/3927>

CLASSICAL SIZE EFFECT IN COPPER THIN FILMS: IMPACT OF SURFACE AND GRAIN  
BOUNDARY SCATTERING ON RESISTIVITY

BY

TIK SUN

B.A. New College of Florida, 2005

A dissertation submitted in partial fulfillment of the requirements  
for the degree of Doctor of Philosophy  
in the Department of Mechanical, Materials, and Aerospace Engineering  
in the College of Engineering and Computer Science  
at the University of Central Florida  
Orlando, Florida

Fall Term

2009

Major Professor: Kevin R. Coffey

@ 2009 Tik Sun

## ABSTRACT

Surface and grain boundary electron scattering contribute significantly to resistivity as the dimensions of polycrystalline metallic conductors are reduced to, and below, the electron mean free path. A quantitative measurement of the relative contributions of surface and grain boundary scattering to resistivity is very challenging, requiring not only the preparation of suitably small conductors having independent variation of the two relevant length scales, namely, the sample critical dimension and the grain size, but also independent experimental quantification of these two length scales. In most work to date the sample grain size has been either assumed equal to conductor dimension or measured for only a small number of grains. Thus, the quantification of the classical size effect still suffers from an uncertainty in the relative contributions of surface and grain boundary scattering.

In this work, a quantitative analysis of both surface and grain boundary scattering in Cu thin films with independent variation of film thickness (27 nm to 158 nm) and grain size (35 nm to 425 nm) in samples prepared by sub-ambient temperature film deposition followed by annealing is reported. Film resistivities of carefully characterized samples were measured at both room temperature and at 4.2 K and were compared with several scattering models that include the effects of surface and grain boundary scattering. Grain boundary scattering is found to provide the strongest contribution to the resistivity increase. However, a weaker, but significant, role is also

observed for surface scattering. Several of the published models for grain boundary and surface scattering are explored and the Matthiessen's rule combination of the Mayadas and Shatzkes<sup>1</sup> model of grain boundary scattering and Fuchs<sup>2</sup> and Sondheimer's<sup>3</sup> model of surface scattering resistivity contributions is found to be most appropriate. It is found that the experimental data are best described by a grain boundary reflection coefficient of 0.43 and a surface specular coefficient of 0.52. This analysis finds a significantly lower contribution from surface scattering than has been reported in previous works, which is in part due to the careful quantitative microstructural characterization of samples performed. The data does suggest that there is a roughness dependence to the surface scattering, but this was not conclusively demonstrated. Voids and impurities were found to have negligible impact on the measured resistivities of the carefully prepared films.

---

<sup>1</sup> A. F. Mayadas and M. Shatzkes, Phys Rev. B **1**, 1382 (1970).

<sup>2</sup> K. Fuchs, Proc. Cambridge Philos. Soc. **34**, 100 (1938).

<sup>3</sup> E. H. Sondheimer, Adv. Phys. **1**, 1, (1952).

Dedicated to my parents:

Late Sun, Oi Charles

Chiu, Siu Man

## ACKNOWLEDGMENTS

First of all I would like to express my gratitude to my advisor, Dr. Kevin R. Coffey, for the support, supervision, guidance, and encouragement. I thank my other committee members, Dr. Katayun Barmak, Dr. Glenn D. Boreman, Dr. Pieter G. Kik, Dr. Yongho Sohn, Dr. Linan An and Dr. Helge Heinrich, for thoughtful discussions and valuable comments.

I wish to acknowledge Advanced Microfabrication Facility (AMF) and the Materials Characterization Facility (MCF) for laboratory support.

I would especially like to thank my group members Andrew Warren and Bo Yao for their assistance with materials characterization in this project. I am also thankful to Edward Dein, Ravi Todi, Amruta Borge, Parag Gadkari, Chaitali China, Prabhu Doss Mani, Matt Erickson, and Vinit Todi for their help and advice along my academic career.

Last, but not the least, I would like to thank my family members who have always believed in me.

# TABLE OF CONTENTS

LIST OF FIGURES	x
LIST OF TABLES	xiv
CHAPTER 1	INTRODUCTION..... 1
1.1	Motivation..... 1
1.2	Electrical Conduction and the Boltzmann Transport Equation ..... 2
1.3	Classical Size Effect ..... 5
1.3.1	Surface Scattering..... 6
1.3.2	Grain Boundary Scattering..... 9
1.4	Challenges..... 11
CHAPTER 2	QUANTITATIVE RESISTIVITY SIZE EFFECT MODELS 14
2.1	Surface Scattering in Thin Films ..... 14
2.2	Roughness Induced Surface Scattering in Thin Films ..... 15
2.3	Grain Boundary Scattering in Thin Films..... 17
2.4	Matthiessen's Rule and Temperature Dependence of the Resistivity Size Effect 19
2.5	Interactions Between Surface and Grain Boundary Scattering..... 22
2.6	Scattering From Impurities and Voids ..... 26
CHAPTER 3	EXPERIMENTAL LITERATURE REVIEW ..... 27
3.1	Introduction..... 27
3.2	Surface Scattering in Single Crystal Metallic Films..... 27
3.3	Combined Surface and Grain Combined Surface and Grain Boundary Scattering





CHAPTER 7	TEMPERATURE DEPENDENCE OF THE CLASSICAL SIZE EFFECT	
		74
CHAPTER 8	SUMMARY, SIGNIFICANCE, AND FUTURE WORK.....	82
APPENDIX A	RESISTANCE INCREASE DUE TO VOID FRACTIONS .....	85
APPENDIX B	PUBLICATION LIST .....	91
REFERENCES		93

## LIST OF FIGURES

FIG. 1-1. Resistance increase of interconnects as line width is reduced below  $0.5 \mu\text{m}$ .<sup>2</sup> ..... 2

FIG. 1-2. Schematic of the Fermi sphere a) under no electric field and b) under an electric field. .... 4

FIG. 1-3. Schematic of electron scattering mechanisms in a copper interconnect line.<sup>17</sup> ..... 8

FIG. 1-4. Electrical Resistivity of Cu thin films as a function of thickness. Cu film deposited on  $\text{SiO}_2$  is fine grained polycrystalline, while that deposited on HF-cleaned Si is composed of large (100) oriented grains.<sup>4</sup> ..... 10

FIG. 2-1 Schematic of Mayadas and Shatzkes where electrons are scattered by step potentials of strength S while grain boundaries parallel to the electric field only scatter specularly. .... 18

FIG. 2-2. A comparison of the temperature dependence of the resistivity increases predicted by the FS ( $\Delta\rho_{\text{FS}}$ , using equation 1a), Soffer ( $\Delta\rho_{\text{Soffer}}$ , using equation 2), and MS ( $\Delta\rho_{\text{MS}}$ , using equation 4a), models are plotted as a function of temperature for a hypothetical polycrystalline Cu thin film having a 30 nm grain size and a 30 nm thickness to illustrate their different temperature dependencies. The temperature dependence of the experimentally measured bulk resistivity,  $\rho$ , of Cu from reference is also shown in the figure.<sup>28</sup> ..... 20

FIG. 2-3 Schematic of electrons incident onto grain boundary assuming interactions with interfaces occur. .... 23

FIG. 2-4. Temperature dependence of the total resistivity of two combined surface and grain

boundary scattering models for a Cu thin film with both a thickness,  $h$ , and a grain size,  $g$ , of 30 nm. The MSS model refers to the model described in equation 5 in which interactions between the two additional scattering mechanisms are considered.<sup>14</sup> The FS+MS model refers to the simple Matthiessen's rule combination (equation 6a) of these two scattering effects. For both models the surface specularity parameter,  $p$ , and the grain boundary reflection coefficient,  $R$ , are set equal to 0.15. .... 25

FIG. 3-1. A plot of normalized resistivity as a function normalized thickness. The unfilled circles are experimental resistivity data points of single crystal  $\text{CoSi}_2$  film from Hensel.<sup>25</sup> ..... 28

FIG. 3-2. The star shape data points and solid line predicting resistivity increase by FS+MS combined models are from Steinhögl et al.'s work.<sup>38</sup> The dash and dotted lines are resistivity predictions from the FS+MS combined models with different specularity and reflection coefficients plotted by Maroms et al. showing the difficulty of extracting meaningful model parameters by analyzing data without independent variations of grain size and line width. .... 32

FIG. 4-1. Determination of void fraction in a field of view in 136.7nm  $\text{SiO}_2/\text{Cu}/\text{SiO}_2$  sample annealed at 150°C, the void area fraction is 0.2 % ..... 40

FIG. 4-2. HCDF image of the 41.7 nm sample annealed at 400°C. .... 42

FIG. 4-3. HCDF images at different tilts of one field of view of an 80 nm sample annealed at 400°C. The red circles indicate a region of grain overlap. .... 43

FIG. 4-4. HCDF image of a 157.9 nm sample annealed at 400°C. The red circles indicate a region of dislocations. .... 44

FIG. 4-5 Comparison of XRR data and fit (red curve) for the 41.7 nm thick Cu film annealed at 400°C. ....	46
FIG. 4-6. Configuration of the Van der Pauw geometry dipping probe .....	47
FIG. 5-1. HAADF transmission electron micrographs of 800°C annealed (30 minutes) 40 nm-thick Cu films encapsulated in Al <sub>2</sub> O <sub>3</sub> with Si/SiO <sub>2</sub> substrate pre-etched by a) Ar+3%H <sub>2</sub> and b) Ar+2%O <sub>2</sub> gas in a biased 30W plasma. ....	51
FIG. 5-2. Bright-field transmission electron micrographs of 800°C annealed Al <sub>2</sub> O <sub>3</sub> /Cu/Al <sub>2</sub> O <sub>3</sub> deposited at a) -40 °C, and b) -120°C. ....	53
FIG. 5-3. Bright-field transmission electron micrograph of 800°C annealed 40 nm thick Cu film encapsulated with 20 nm of Al <sub>2</sub> O <sub>3</sub> deposited (a) in 2mT Ar+3%H <sub>2</sub> (b) 8mT Ar+3%H <sub>2</sub> (c) 16mT Ar+3%H <sub>2</sub> .....	54
FIG. 5-4. Bright-field transmission electron micrograph of 800°C annealed 40 nm thick Cu film encapsulated with 20 nm of Al <sub>2</sub> O <sub>3</sub> deposited (a) without bias and (b) with 30 W bias. ....	55
FIG. 5-5. Bright-field transmission electron micrograph of 400 °C annealed 20 nm Cu film encapsulated in Al <sub>2</sub> O <sub>3</sub> (a) annealed in a reducing gas of Ar+3%H <sub>2</sub> , (b) in a non-reducing gas, for 40 minutes .....	56
FIG. 5-6. Bright-field transmission electron micrograph of 40 nm Cu film encapsulated in 20 nm of Al <sub>2</sub> O <sub>3</sub> (a) annealed at 800 °C and (b)1000 °C in Ar+3%H <sub>2</sub> for 40 minutes .	58
FIG. 5-7. Bright-field transmission electron micrograph of 40 nm Cu films encapsulated in 20 nm of Al <sub>2</sub> O <sub>3</sub> annealed at 800 °C for (a) 10 seconds (b) 40 minutes and (c) 160 minutes. ....	59

FIG. 6-1. Cross-sectional and HCDF plan-view transmission electron micrograph of 36.9 nm Cu film encapsulated in 20 nm of SiO<sub>2</sub> with 2nm of Ta liners annealed at 600 °C. .... 62

FIG. 6-2. Plot of grain sizes of Cu thin films as a function of Cu layer thickness for the sixteen SiO<sub>2</sub>/Cu/SiO<sub>2</sub> and six SiO<sub>2</sub>/Ta/Cu/Ta/SiO<sub>2</sub> samples studied in this work. The open circles show an example of an ideal data set, without correlation between the two variables, and the filled circles are the experimental data from Table 1. .... 63

FIG. 6-3. The room temperature resistivity of SiO<sub>2</sub>/Cu/SiO<sub>2</sub> and SiO<sub>2</sub>/Ta/Cu/Ta/SiO<sub>2</sub> thin films a) as a function of Cu layer thickness,  $h$ , and b) as a function of Cu layer grain size,  $g$ . The data points correspond to the samples listed in Table 1. The solid curve corresponds to the FS model (equation 1a) in (a) and MS (equation 4a) model in (b). 64

FIG. 6-4. The 4.2 K resistivity of SiO<sub>2</sub>/Cu/SiO<sub>2</sub> and SiO<sub>2</sub>/Ta/Cu/Ta/SiO<sub>2</sub> thin films a) as a function of Cu layer thickness,  $h$ , and b) as a function of Cu layer grain size,  $g$ . The data points correspond to the samples listed in Table 1. The solid curve corresponds to the FS model (equation 1a) in (a) and MS (equation 4a) model in (b). .... 69

FIG. 7-1. The resistivity increase of SiO<sub>2</sub>/Cu/SiO<sub>2</sub> and SiO<sub>2</sub>/Ta/Cu/Ta/SiO<sub>2</sub> thin films due to size effect ( $\Delta\rho$ ) plotted as a function of Cu layer grain size,  $g$ . The filled symbols are resistivities measured at room temperature, and the open symbols are resistivities measured at 4.2 K. The data points correspond to the samples listed in Table 1. The solid curve corresponds to the resistivity size effect due to MS grain boundary scattering ( $\Delta\rho_{MS}$ ). .... 75

FIG. 7-2. Schematic of the FS+MS combined model where no interaction occurs between grain boundary and surface at low temperature. .... 81

## LIST OF TABLES

Table 1 Annealing temperature, thickness, root mean square roughnesses (upper, $r_1$ , and lower, $r_2$ , of the Cu/encapsulant layer interfaces), 296 K and 4.2 K resistivity, and grain size data for SiO <sub>2</sub> -encapsulated Cu thin films (Table 1a), and the Ta/SiO <sub>2</sub> -encapsulated Cu thin film (Table 1b). .....	38
Table 2. Grain size and void area fraction of 40 nm-thick Cu films encapsulated in 20 nm-thick films of four dielectric encapsulation materials. The films were annealed at 400°C or 800°C.....	57
Table 3. A summary of classical modes, model fitting SSE's, and model fitting parameters. ....	66
Table 4. A summary of classical models, model fitting SSE's, and model fitting parameters for samples measured at 4.2 K. ....	71
Table 5. A summary of classical models, model fitting SSE's, and model fitting parameters for data at RT and 4.2 K.....	77

# CHAPTER 1 INTRODUCTION

## 1.1 Motivation

It has been long known that the resistivity of a conductor increases sharply as its dimensions reduce to its electron mean free path,<sup>1</sup> the average distance an electron travels before it is scattered by lattice thermal vibrations (phonons). The importance of this effect to polycrystalline metal interconnects in silicon technology was first identified in 1998 by Chen and Gardner, and is shown in FIG. 1-1.<sup>2</sup> This resistivity increase has a major impact on the microelectronics industry. The International Technology Roadmap for Semiconductors predicts that the typical line-width for the first layer of wiring in the back-end-of-the-line interconnects (a.k.a. the Metal 1 Wiring Pitch) will be 90 nm in 2010,<sup>3</sup> and the classical size effect is expected to cause a 2X increase in line resistivity.<sup>4</sup> Such an increase in line resistivity will severely limit interconnect conductance and negatively impact integrated circuit performance.<sup>5, 6, 7</sup> Further, as the microelectronics industry scales the Metal 1 Wiring Pitch towards 64 nm by 2013, the need to overcome the resistivity size effect becomes more urgent. Consequently, the size effect in Cu conductors has been identified by ITRS as a “Grand Challenge” problem to be solved in this decade and in the next.<sup>3</sup> To enable optimum scaling of high performance nano-interconnects for ULSI applications at and below the 45 nm design node, it is important to gain insight into the physical origins of this conductivity degradation.



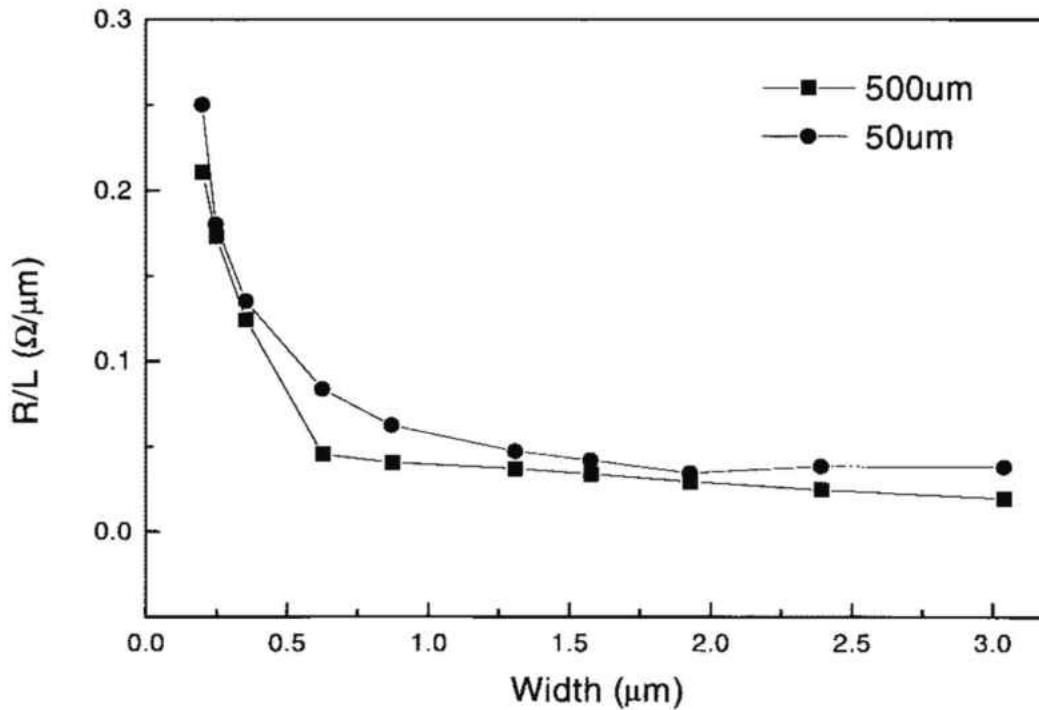


FIG. 1-1. Resistance increase of interconnects as line width is reduced below 0.5  $\mu\text{m}$ .<sup>2</sup>

## 1.2 Electrical Conduction and the Boltzmann Transport Equation

The Boltzmann transport theory is a useful context for understanding the basic of electrical conduction in metals and will be introduced very briefly here.

Within a metal, the conduction electrons at the Fermi surface are moving at the Fermi velocity, which is  $1.57 \times 10^6$  m/s in Cu.<sup>8</sup> Electrons at lower energy states within the Fermi surface are also moving, but at lower velocities. As all of the electrons are moving in all possible directions, the net velocity of the distribution of the electrons is zero (i.e., for each electron moving to the left, there is a comparable state with an equal probability of occupation for an electron moving to the right). In momentum space, the shape of the Fermi surface is

commonly assumed to be spherical (this is a reasonable approximation for Cu) as depicted in FIG. 1-2. If the metal is subjected to an applied DC electric field, all of the electrons will accelerate at a constant rate and the net effect would be an indefinitely increasing displacement of the Fermi sphere to the opposite direction. However, at room temperature, the lattice vibrations in metals (phonons) or impurities and other defects scatter the electrons between states and result in a net shift of electrons from the non-equilibrium higher energy states on the right edge of the shifted sphere into the lower energy states on the left edge on the shifted sphere, acting to restore the Fermi sphere to its equilibrium condition. As a result of this scattering, the extent of the shift of the Fermi sphere does not increase indefinitely and reaches a steady state condition where the effect of electric field to shift the sphere is balanced by the electron scattering events, as shown in FIG. 1-2 (a). The steady state net current that results from the displacement of the Fermi sphere is a result of the electrons on the right edge with positive x-axis momentum not being matched by electrons in occupied states on the left edge. Qualitatively, for the same applied electric field, less frequent scattering (weaker restoring force) allows a greater steady state shift of the Fermi sphere and hence a greater net electric current. Thus, a material's electrical conductivity can be related to shape and density of state near its Fermi surface, and the extent to which the Fermi surface may be shifted in the presence of an electric field. When the electric field is turned off, the Fermi sphere will be returned to its original equilibrium position by the electron scattering (FIG. 1-2) a) and the net current will cease.

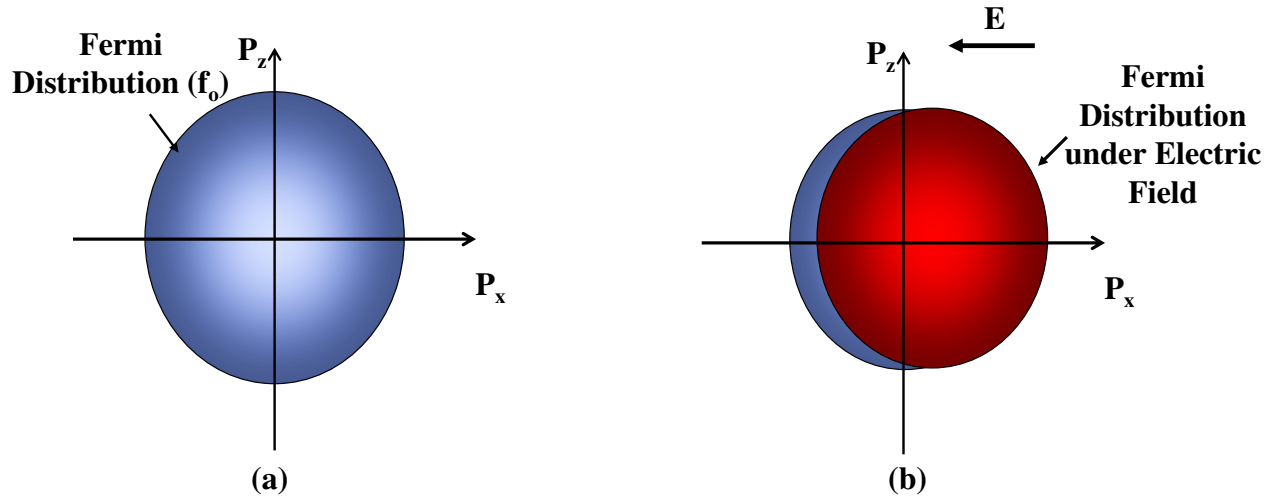


FIG. 1-2. Schematic of the Fermi sphere a) under no electric field and b) under an electric field.

Quantitatively, this model of transport of electrons in metals is commonly described by the Boltzmann Transport Equation:

$$\frac{\partial f}{\partial t} = -v_x \frac{\partial f}{\partial z} + \frac{q\varepsilon_x}{\hbar} \frac{\partial f}{\partial k_x} + \frac{\partial f}{\partial t} \Big|_{coll} ,$$

where  $f$  is the Fermi distribution,  $t$  is time,  $v_x$  is the velocity of the electron along the  $x$  direction,  $\varepsilon_x$  is the electric field along  $x$  direction,  $k_x$  is the wave vector along the  $x$  direction,  $\hbar$  is the

Planck's constant, and  $\frac{\partial f}{\partial t} \Big|_{coll}$  is the change of the Fermi distribution. The Fermi distribution

is a function of the three electron momentum components (that, with spin, describe a unique electron state) and time. As a result, the Fermi distribution describes which states are occupied or not, and hence can be used to calculate the net current (e.g., if more higher energy/velocity

states on the left edge of the sphere are occupied than on the right edge, a net current will be present. At equilibrium in normal metals, the Fermi distribution is symmetric and there is no net current. Changes in the distribution function are driven by changes in electron concentration and kinetic energy, by the acceleration of the electrons due to an applied electric field, and by scattering events. In steady state conditions, these effects necessarily balance and  $\frac{\partial f}{\partial t}$  equals to zero.

### 1.3 Classical Size Effect

The classical size effect differs from the quantum size effect in that the confinement dimension is larger than the De Broglie Wavelength, such that electron states are continuous.<sup>9</sup> For the quantum size effect to be observed, an electron must be spatially confined in at least one dimension such that the variance of momentum is large and there is a resultant large band gap for a collection of electrons. Quantum size effects provide for significant changes in transport properties due to the deviation of the electron states from those of a three dimensional solid. In contrast, the classical size effect is observed when the quantum states of a three dimensional solid still apply, but a confinement has occurred wherein the conductor is smaller than the electron mean free path, in at least one dimension. This provides for modifications of the conductivity of solids that can be treated within the context of Boltzmann transport theory.<sup>9</sup>

Considerable work has been done in the field of electron transport over the past 100 years, and four electron scattering mechanisms have been subsequently identified to contribute to the classical size effect: surface scattering, grain boundary scattering, impurity scattering, and roughness<sup>4,10,11,12,13,14,15</sup>. In the 30 to 45 nm regime, it has been established that the effect of

roughness and impurity scattering can be negligible in the case of annealed Cu lines of sufficiently high purity.<sup>10</sup> One of the key remaining questions is whether surface scattering or grain boundary scattering is the dominant mechanism<sup>16,17</sup> and it is the goal of this research to provide a definitive answer to that question in high purity Cu.

### 1.3.1 Surface Scattering

The primary resistivity mechanism in metals at room temperature is the scattering of conduction electrons by phonons (lattice vibrations). This scattering results in the loss of the additional energy and momentum that the electron may have gained from an applied electric field and hence impedes the electron response to the applied field, i.e, provides for metallic resistivity. The average distance that an electron travels between such scattering events is termed the electron mean free path. Electrons may also be similarly scattered by impurities, planar and linear defects in crystals, and the conductor's external surfaces. As the smallest dimension of the conductor is reduced to the order of its electron mean free path, the electric field induced momentum loss due to scattering of electrons by the external surfaces of the conductor (or other defects) increases and gives rise to the classical resistivity size effect. Fuchs<sup>13</sup> was the first to explain and model the effect in the context of scattering at the top and bottom surfaces of thin films. Sondheimer<sup>14</sup> later extended Fuchs' work to narrow metal lines. Collectively, their theory of surface scattering is known as the Fuchs and Sondheimer (FS) model. Derived from the Boltzmann transport equations, the FS model treats all scattering events at the conductor surfaces to be either "diffuse" or "specular." The FS model assigns a fixed probability,

$p$ , for specular scattering events to occur and  $1-p$  becomes the probability that diffuse scattering events. This specular scattering probability is the sole characteristic of the external surface considered by the model. In a diffuse scattering event, any additional field induced velocity of the electron is lost upon collision of the surface and the electron. In terms of the displacement of the Fermi sphere, diffuse surface scattering has a similar result to that of phonon scattering, in that electrons from the higher energy states of the shifted Fermi surface (right edge in Figure 1-2 (a)) are scattered into the lower energy states (left edge) and thus the net shift of the Fermi surface is reduced. However, it should be noted that phonon scattering is effectively isotropic in polycrystalline metals, while diffuse surface scattering is not. Specifically, if the external surface of a film are taken as parallel to the x-y plane, then it can be expected that diffuse surface scattering will more strongly effect electrons with significant z-axis momentum components while electrons with nearly zero z-axis momentum will travel parallel to the surfaces and only interact with the surface infrequently. In a specular scattering event, a conduction electron incident upon the external surface is reflected with no change in its energy while its momentum perpendicular to the plane of the film is reversed, i.e., any electric field induced momentum in the field plane is preserved. In terms of the Fermi sphere, such scattering results in a change in sign of the electron's z-axis momentum, but does not serve to restore the position of the Fermi sphere to equilibrium as it does not change the x-axis component of electron momentum.

FIG. 1-3. is a schematic of electron conduction in a Cu interconnect line with a TaN/Ta-barrier layer within a SiO<sub>2</sub> and Si<sub>3</sub>N<sub>4</sub> layered matrix.<sup>18</sup> The blue arrows at the top of the Cu line illustrate the two possible scattering events at the surface. The electron incident on the external surface is illustrated by the first dark blue arrow and the specularly scattered electron

trajectory is illustrated by the second dark blue arrow. The shorter light blue arrows pointing towards various directions are possible electron trajectories for the case of diffuse scattering from the surface. It should be noted that the resistivity increase in thin films and lines is only due to diffuse scattering under the FS theory. As the Cu-lines (or films) become narrower, the number of surface scattering events increases and their contribution to the total conductor resistivity increases, as shown in FIG. 1-1.

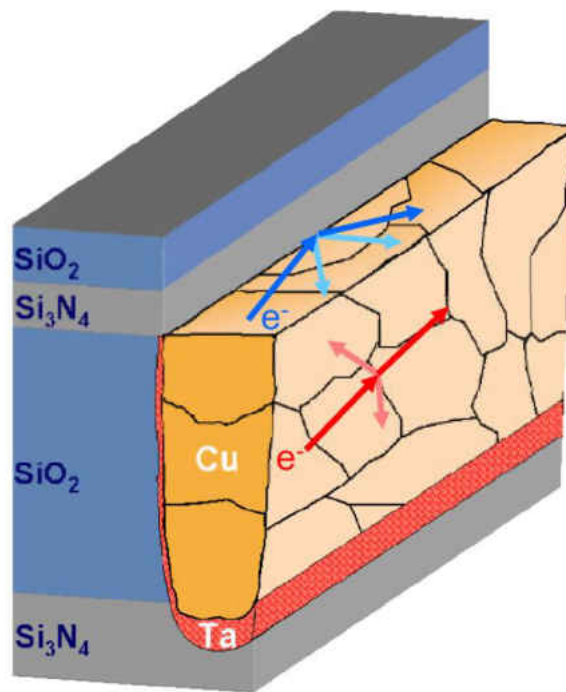


FIG. 1-3. Schematic of electron scattering mechanisms in a copper interconnect line.<sup>18</sup>

A number of researchers<sup>19,20</sup> took issue with Fuchs' assumption of constant specularity for the

electron/interface interaction, which ignores the electron wavelength, the incident angle, and the interface roughness. For example, Soffer<sup>21</sup> proposed an alternative surface scattering model based on flux conservation that attributes the resistivity size effect mostly to electrons incident onto rough surfaces at non-grazing angles.

### 1.3.2 Grain Boundary Scattering

For more than 30 years, surface or roughness-induced surface scattering were considered the only mechanisms contributing to classical size effect. In 1970, Mayadas and Shatzkes<sup>15</sup> observed that the resistivity size effect was more significant in polycrystalline conductors in comparison to that in single crystals. A more recent example of this is shown in FIG. 1-4, from the work of Rosnagel and Kuan.<sup>4</sup> It is evident that there is an additional ~30% resistivity size effect in polycrystalline Cu films deposited on SiO<sub>2</sub> over that of single crystal (100) Cu films deposited on (100) Si.<sup>4</sup> Mayadas and Shatzkes<sup>15</sup> (MS) explained and modeled this additional resistivity size effect in terms of grain boundary scattering, i.e., the grain boundaries in polycrystalline conductors can also scatter electrons and contribute to a resistivity size effect. When the grain size of a polycrystalline conductor is of the order of the conductor's electron mean free path, it may be scattered by the grain boundaries that separate crystals with different orientations in polycrystalline materials. The MS model considered that all interactions of conduction electrons with the grain boundary would result in either reflection, with a probability  $R$ , or transmission, with a probability  $I-R$ . FIG. 1-3 shows an electron incident upon a grain boundary as a dark red arrow and the transmitted electron trajectory as a second dark red arrow. The light red arrows are possible trajectories of reflected electrons. Transmitted electrons maintain their electric field induced momentum, and hence these events do not contribute to a



resistivity size effect. Reflected electrons lose their field induced momentum and contribute to a size effect resistivity increase when the grain size of the conductor is reduced. In terms of the Fermi sphere displacement, the reflected electrons are scattered similarly to electrons scattered by phonon, in that they are considered to be scattered from the high energy states (right edge in figure 1-2 b) to the lower energy states (left edge) and this serves to restore the equilibrium Fermi distribution. Grain boundary scattering is also not isotropic, and, as modeled, primarily scatters electrons with momentum components parallel to the applied field.

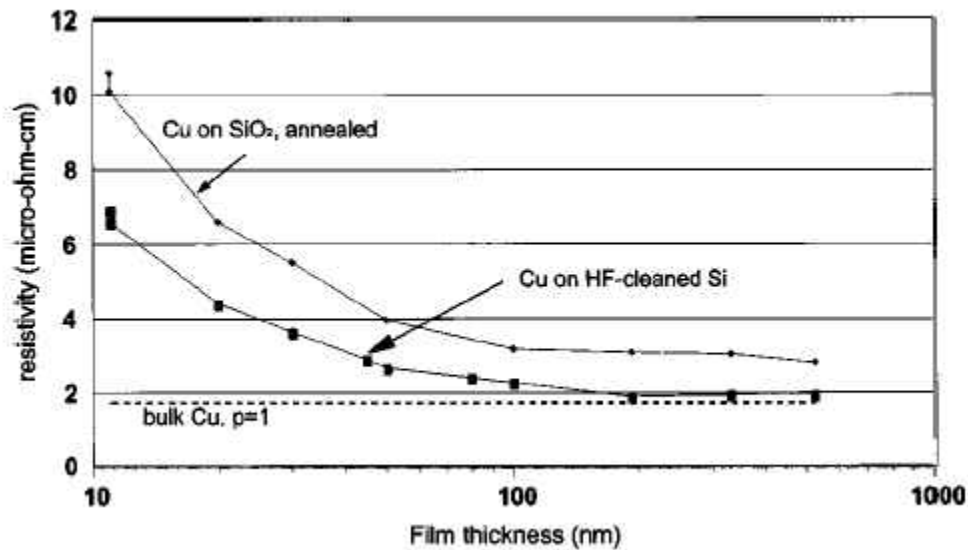


FIG. 1-4. Electrical Resistivity of Cu thin films as a function of thickness. Cu film deposited on SiO<sub>2</sub> is fine grained polycrystalline, while that deposited on HF-cleaned Si is composed of large (100) oriented grains.<sup>4</sup>

## 1.4 Challenges

As aforementioned, researchers initially considered the scattering of the conduction electrons from the top and bottom surfaces of the film as the primary mechanism contributing to the size effect. More recently, grain boundary scattering has also been recognized as a significant factor affecting resistivity. Since thinner films and wires tend to also have smaller grains, both mechanisms can progressively increase the resistivity of thinner polycrystalline films. The fundamental problem faced by all who wish to model, or, more importantly, eliminate this resistivity increase in polycrystalline metal films is that the classical size effect is due to this combination of electron scattering mechanisms. Both surface and grain boundary scattering clearly play an important role in the classical size effect, but the relative importance of these mechanisms has been difficult to quantify.<sup>17</sup> Even recent works within the interconnect community echo the older, and often conflicting reports attributing the dominant mechanism of the size effect to either surface,<sup>22</sup> or to grain boundary scattering,<sup>23</sup> or even to an increase in film contamination as the linewidth is reduced. Two factors contribute to this controversy. First, both grain boundary and surface scattering are expected to give a similar functional form, wherein the resistivity increase is inversely proportional to “x”, where “x” is the grain size or film thickness/linewidth. Second, any decrease in film thickness or linewidth of polycrystalline samples has been experimentally accompanied by a decrease in grain size, confounding these two effects. As a consequence, surface scattering and grain boundary scattering in polycrystalline thin films cannot be studied separately. In light of these two factors, it can be fairly said that a credible assessment of the relative importance of surface and grain boundary scattering in thin films had not been accomplished prior to the work described in this dissertation.

In addition to surface and grain boundary scattering, the resistance of polycrystalline thin films can also be increased by the presence of impurities and voids. Higher concentrations of impurities, such as Al, O and C, have been observed in thin films. A typical resistivity increase attributed to impurity scattering in high purity ( $\geq 99.99\%$ ) Cu thin films has been reported to be about  $0.01\mu\Omega\text{-cm}^{24}$ , and the temperature dependence of impurity scattering has been well studied and is described by Matthiessen's rule, the simple addition of the resistivities associated with different mechanisms. Voids are also often found in thin films as a by-product of processing, and while not directly affecting resistivity, voids can result in errors in the measurements of sheet resistance that are used to calculate resistivity experimentally. An example of this is Hensel's experimental data<sup>25</sup> of apparently increased resistivity for thinner epitaxial  $\text{CoSi}_2$  films, which he attributed to a reduced quality (pinholes) of his thinnest silicide films. As the resistivity errors expected from low levels of voiding was not available in the literature, a brief description is provided in Appendix A.

The applicability of Matthiessen's rule is another important issue in understanding the resistivity of nanoscale conductors. Although Matthiessen's rule is useful to describe the combined effects of impurity and phonon scattering, it is not expected to be applicable to scattering from planar defects (such as grain boundaries and film exterior surfaces), because the mean free path is now dependent on the angle at which the electron is incident upon the defect.<sup>12</sup> Further, significant deviations from Matthiessen's rule have been previously reported in studies of the classical resistivity size effect.<sup>26</sup> Accordingly, for an understanding of grain boundary and surface scattering, we must consider these two scattering effects together, in addition to taking into

account the bulk scattering mechanisms.

## CHAPTER 2

## QUANTITATIVE RESISTIVITY SIZE EFFECT MODELS

In the last chapter, the various scattering mechanisms which contribute to the resistivity size effect were qualitatively discussed. The quantitative physical models proposed for these mechanisms will be the focus of this chapter. In particular, the assumptions, the critical parameters, the limits, and the applicability of these physical models will be examined in detail. Further, the manner in which the various scattering mechanisms are integrated will be discussed.

### 2.1 Surface Scattering in Thin Films

Fuchs and Sondheimer's (FS) model of surface scattering, derived from the Boltzmann transport equation, took the semi-classical approach of Sommerfeld's<sup>Error! Bookmark not defined.</sup><sup>24</sup> description in which electrons would have a limited mean free path as a result of phonon and impurity scattering. This assumption is in contrast to the infinite mean free path in Drude-Lorentz's free electron theory.<sup>Error! Bookmark not defined.</sup><sup>24</sup> The specular coefficient,  $p$ , describes the fraction of electrons that will be specularly scattered at the film surface, upon specular scattering, the electron velocity perpendicular to the film surface ( $v_z$ ) is reversed in sign while the drift velocity (velocity gained from the electric field) is conserved. The remaining  $(1-p)$  fraction of the scattered electrons will undergo diffusive scattering, during which electrons will lose their drift velocity. It is important to note that the model is highly artificial and ignores the microstructural details and non-extreme cases of scatterings at the surface. The important length scales in the FS model are the conductor's dimension(s) perpendicular to the

current flow (i.e., for a thin film, the thickness,  $h$ ) and the mean free path of the conduction electrons due to phonon and impurity scattering,  $\lambda$ . The FS model describes the resistivity ( $\rho_{\text{FS}}$ ) of a thin film as:<sup>13</sup>

$$\rho_{\text{FS}} = \rho_i \left[ 1 - \left( \frac{3}{2k} \right) (1-p) \int_1^{\infty} \left( \frac{1}{t^3} - \frac{1}{t^5} \right) \frac{1 - \exp(-kt)}{1 - p \exp(-kt)} dt \right]^{-1}, \quad (1a)$$

where  $k = h/\lambda$  and  $\rho_i$  is the bulk resistivity of the metal. At room temperature, the bulk resistivity is primarily determined by phonon scattering while at low temperatures (4.2 K) it is primarily determined by residual crystalline defects. In the limits of small  $k$ , equation 1a is simplified to:

$$\rho_{\text{FS}} = \rho_i \left[ 1 + \left( \frac{3}{8} \right) \frac{\lambda}{h} (1-p) \right] \quad (1b)$$

Equation 1b is often used for the empirical analysis of resistivity versus thickness data. In this dissertation, it is convenient to consider the resistivity increase predicted by this model as  $\Delta\rho_{\text{FS}}$ , which is given by  $\Delta\rho_{\text{FS}} = \rho_{\text{FS}} - \rho_i$ .

## 2.2 Roughness Induced Surface Scattering in Thin Films

The FS model uses the specular reflection probability,  $p$ , as a characteristic of the conductor's external surface that can be varied to fit experimental data, but does not explicitly include the roughness of the scattering surface. Soffer introduced a surface scattering model that uses the roughness of the scattering surface to calculate an angle-dependent specular reflection

probability.<sup>21</sup> This model allows for comparison to experimental data with no fitting parameters when the roughness of the scattering surfaces is known. For a thin film with top surface (1) and bottom surface (2) having separate root mean square roughnesses,  $r_1$  and  $r_2$ , the Soffer specular reflection probability for each surface is given by:<sup>21</sup>

$$p_1(\cos \theta) = \exp\left[-\left(\frac{4\pi r_1}{\lambda_F}\right)^2 \cos^2(\theta)\right] \quad p_2(\cos \theta) = \exp\left[-\left(\frac{4\pi r_2}{\lambda_F}\right)^2 \cos^2(\theta)\right],$$

where  $\theta$  is the angle of incidence of the electrons to the conductor's surface and  $\lambda_F$  is the electron wavelength at the Fermi surface, about 0.5 nm for Cu.<sup>23</sup> The average specularity parameter for the top and bottom surfaces in the Soffer model is given as:

$$\overline{p(\cos \theta)} = \frac{1}{2} [p_1(\cos \theta) + p_2(\cos \theta)]$$

and Soffer's resistivity size effect model is then:<sup>27</sup>

$$\rho_{\text{Soffer}} = \rho_i \left\{ 1 - \left(\frac{3}{2k}\right) \int_0^1 \frac{(u-u^3) \left[ 1 - \exp\left(-\frac{k}{u}\right) \right] \left\{ 1 - \overline{p}(u) + [\overline{p}(u) - p_1(u)p_2(u)] \exp\left(-\frac{k}{u}\right) \right\}}{\left[ 1 - p_1(u)p_2(u) \exp\left(-\frac{2k}{u}\right) \right]} du \right\}^{-1} \quad (2)$$

Using this model, the increase in resistivity due to surface roughness induced scattering is thus:

$$\Delta\rho_{\text{Soffer}} = \rho_{\text{bulk}} - \rho_{\text{Soffer}}.$$

More recently, Rossnagel and Kuan (RK)<sup>4</sup> proposed a semi-empirical extension of the FS model to include surface roughness explicitly. Based on Monte-Carlo simulations of electron trajectories near a rough surface, their resistivity model is given by:

$$\rho_{\text{RK}} = \rho_i + \Delta\rho_{\text{FS}} \left( 1 + \frac{r_1}{n} \right) \quad (3)$$

where  $n$  incorporates the conductor thickness and Fermi wavelength and is determined by Monte-Carlo simulations of electron trajectories. This model continues to use the specular coefficient of the FS model as a single fitting parameter and allows for larger resistivity increases than the FS model.

### 2.3 Grain Boundary Scattering in Thin Films

Mayadas and Shatzkes<sup>15</sup> developed an extension of the Boltzmann transport theory to include reflection and transmission of conduction electrons at the grain boundaries of a polycrystalline metal. Their model assumes that grain boundaries are all either parallel or perpendicular to the direction of current flow and that electrons incident upon the parallel grain boundaries are only specularly reflected, i.e., the parallel grain boundaries have no role in the resistivity size effect. Each perpendicular grain boundary is treated as an internal surface, and when a conduction electron collides with the grain boundary, it has a probability of transmission or reflection that is quantified by a reflection coefficient,  $R$  (FIG. 2-1). This coefficient is allowed to take values between zero and one and is commonly varied to fit experimental data.



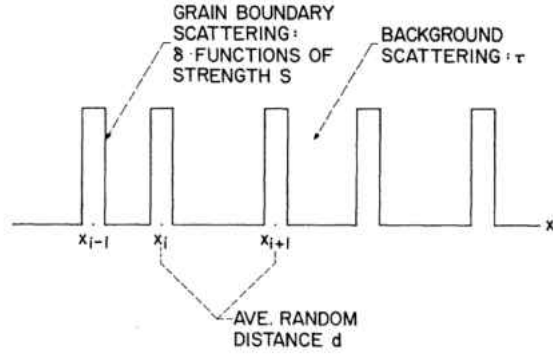


FIG. 2-1 Schematic of Mayadas and Shatzkes where electrons are scattered by step potentials of strength  $S$  while grain boundaries parallel to the electric field only scatter specularly.

The important length scales for this model are the average grain size,  $g$ , and the electron mean free path,  $\lambda$ . The parameters  $R$ ,  $g$ , and  $\lambda$  are conveniently combined as  $\alpha = \left(\frac{\lambda}{g}\right) \frac{R}{(1-R)}$  and the MS model describes the resistivity ( $\rho_{MS}$ ) of a film as:<sup>15</sup>

$$\rho_{MS} = \rho_i \left[ 1 - \frac{3}{2}\alpha + 3\alpha^2 - 3\alpha^3 \ln\left(1 + \frac{1}{\alpha}\right) \right]^{-1} \quad (4a)$$

In the limits of small  $\alpha$ , equation 4a is reduced to:

$$\rho_{MS} = \rho_i \left[ 1 + \left(\frac{3}{2}\right) \left(\frac{\lambda}{g}\right) \left(\frac{R}{1-R}\right) \right] \quad (4b)$$

Using the MS model, the increase in resistivity due to grain boundary scattering is  $\Delta\rho_{MS} = \rho_{MS} - \rho_i$ . Equations (1b) and (4b) can be seen to have a fundamentally similar form, namely  $\rho(x) = \rho_i + A/x$ , where  $x$  is the experimentally varied size parameter (grain size or film

thickness) and  $A$  is a constant, typically determined by fitting to the experimental data. Given the tendency in polycrystalline thin films for the grain size and the film thickness to be nearly equal or at least proportional (i.e.,  $h \propto g$ ) the resistance increase associated with the classical size effect can be attributed to either mechanism when both effects are present. When the resistivity data comes from samples lacking independent variation of grain size and thickness, different pairs of  $p$  and  $R$  can provide the same value for the fitting constant,  $A$ , and thus fit the experimental data equally well.

## 2.4 Matthiessen's Rule and Temperature Dependence of the Resistivity Size Effect

An additional issue to consider for the quantitative modeling of the resistivity size effect is the applicability of Matthiessen's rule. Impurity scattering and phonon scattering, as well as grain boundary and surface scattering, are often included in the modeling of resistivity size effects by the use of Matthiessen's rule. Landauer<sup>12</sup> has pointed out that planar scattering defects (i.e., surfaces and grain boundaries) may not follow this rule, even though isotropic point scattering centers (impurities, phonons) do. Experimentally, significant deviations from Matthiessen's rule have been reported in studies of the classical resistivity size effect.<sup>26</sup> In FIG. 2-2,  $\Delta\rho_{FS}$ ,  $\Delta\rho_{MS}$ ,  $\Delta\rho_{\text{Surface}}$ , (as calculated from the above models) and  $\rho_1$  (from published experimental data)<sup>28</sup> are plotted as a function of temperature for a hypothetical film sample having a 30 nm grain size and a 30 nm thickness. Different temperature dependence is predicted for surface and grain boundary scattering. As can be seen in the figure,  $\Delta\rho_{MS}$  increases only  $\sim 5\%$  over the temperature range of

10 K to room temperature, while both  $\Delta\rho_{\text{FS}}$  and  $\Delta\rho_{\text{Soffer}}$  increase by more than 60%, even though both grain size and thickness are held constant. From this it can be immediately concluded that Matthiessen's rule can not be used to combine the resistivity contributions of surface and phonon scattering, as a significant interaction between these mechanisms is predicted. A number of experimental works have attempted to use the predicted temperature dependencies to separate the contributions of grain boundary scattering and surface scattering to the resistivity increase by comparing the experimental resistivity data over a range of temperatures.<sup>22, 29</sup>

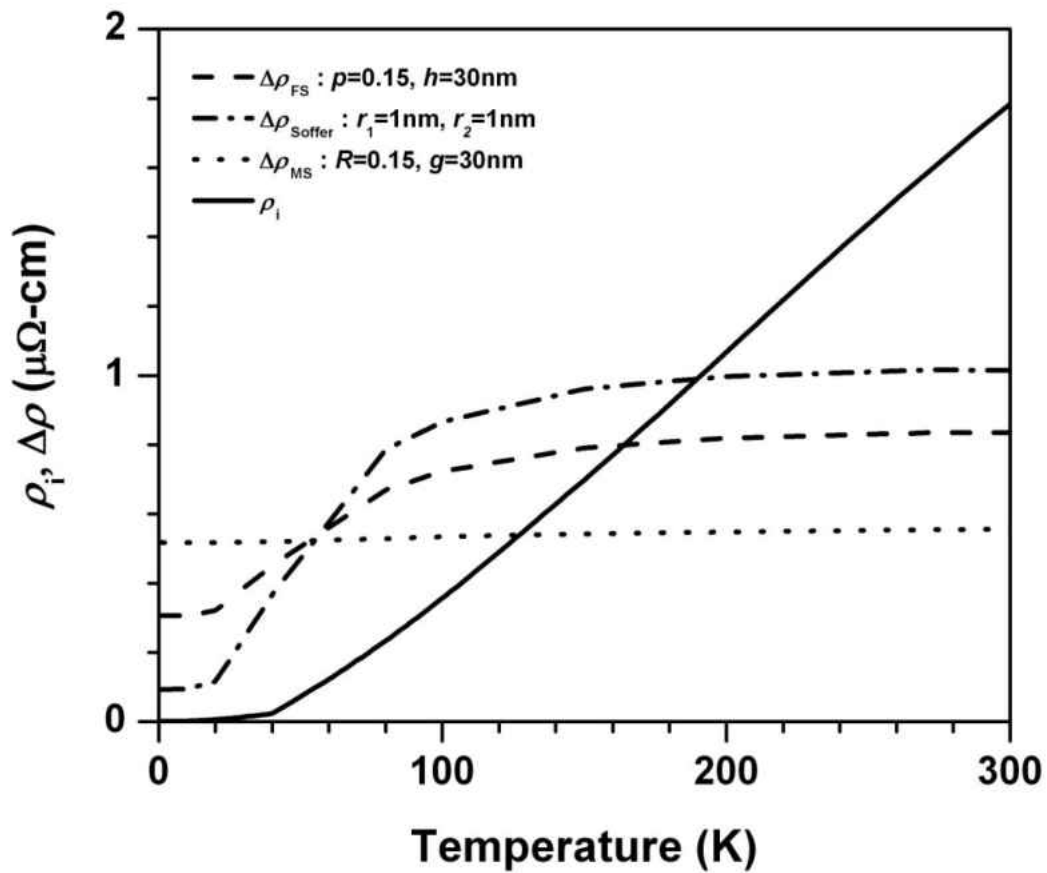


FIG. 2-2. A comparison of the temperature dependence of the resistivity increases predicted by the FS ( $\Delta\rho_{\text{FS}}$ , using equation 1a), Soffer ( $\Delta\rho_{\text{Soffer}}$ , using equation 2), and MS ( $\Delta\rho_{\text{MS}}$ , using equation 4a), models are plotted as a function of temperature for a hypothetical polycrystalline Cu thin film having a 30 nm grain size and a 30 nm thickness to illustrate their different temperature dependencies. The temperature dependence of the experimentally measured bulk resistivity,  $\rho$ , of Cu from reference is also shown in the figure.<sup>28</sup>

The large dependence of  $\Delta\rho_{\text{FS}}$  and  $\Delta\rho_{\text{Soffer}}$  on temperature is due to the interaction between the surface scattering and phonon scattering that is inconsistent with Matthiessen's rule. Matthiessen's rule would require the simple addition of a constant surface or constant grain boundary resistivity contribution with the phonon contribution to provide the total resistivity. It should also be noted that the temperature dependence predicted for the FS ( $\Delta\rho_{\text{FS}}$ ) and Soffer ( $\Delta\rho_{\text{Soffer}}$ ) models differ significantly (~40%), even though a common physical mechanism is invoked. Surface scattering clearly shows a stronger interaction with phonon scattering (temperature dependence) than does grain boundary scattering and this is readily understood. Increased phonon scattering allows the fraction of electrons with momentum parallel to the external surfaces to be more frequently redirected towards the surfaces, resulting in an increase in surface scattering as phonon scattering is increased (as temperature is increased). For grain boundary scattering, the electrons responsible for the current flow cannot avoid impinging on grain boundaries, and, therefore, phonon scattering, and thus temperature, have a small effect on the resistivity. In developing their model, Mayadas and Shatzkes assumed that the grain boundaries parallel to the current flow provided purely specular scattering of electrons. If these

parallel boundaries were alternatively assumed to have a partially diffuse scattering character, they would provide a resistivity contribution that would be increased by phonon scattering and have similar temperature dependence as that of surface scattering. Such a resistivity contribution would scale with average grain size, rather than with sample thickness. As will be shown later, this hypothesis is readily tested by comparison to experimental data wherein a MS-type scattering model having different reflection coefficients at different temperatures is considered. This approach will be referred to as the MST model when separate reflection coefficients for the RT and 4.2 K data are considered.

## **2.5 Interactions Between Surface and Grain Boundary Scattering**

As discussed before, Matthiessen's rule is not valid for combining surface and phonon scattering. The next question is whether surface and grain boundary scattering can be combined using Matthiessen's rule. An interaction between surface and grain boundary scattering is, in fact, expected at low temperatures, wherein grain boundary scattering serves, instead of phonon scattering, to scatter the electrons with momentum parallel to the external field to be more frequently redirected towards the external surfaces as shown in FIG. 2-3. This view was shared by Mayadas and Shatzkes. In addition to providing their model for grain boundary and phonon scattering, Mayadas and Shatzkes<sup>15</sup> derived a more complex model that combines the scattering effects of grain boundaries, external surfaces, and phonons in polycrystalline metallic films. The total film resistivity of the Mayadas Shatzkes Surface model (MSS) is computed as<sup>15</sup>:

$$\rho_{\text{MSS}} = \left[ \frac{1}{\rho_{\text{MS}}} - \left( \frac{6}{\pi k \rho_i} \right) (1-p) \int_0^{\frac{\pi}{2}} d\phi \int_1^{\infty} dt \frac{\cos^2 \phi}{H^2(t, \phi)} \left( \frac{1}{t^3} - \frac{1}{t^5} \right) \frac{1 - \exp[-ktH(t, \phi)]}{1 - p \exp[-ktH(t, \phi)]} dt \right]^{-1} \quad (5)$$

where  $H(t, \phi) = 1 + \frac{\alpha}{\cos \phi \sqrt{1 - \frac{1}{t^2}}}$ . For a single crystal film ( $\alpha=0$ ), equation (5) reduces to

equation (1a). For polycrystalline thin films, equation (5) includes the resistivity increase due to grain boundary scattering redirecting some of the electrons towards the surfaces.

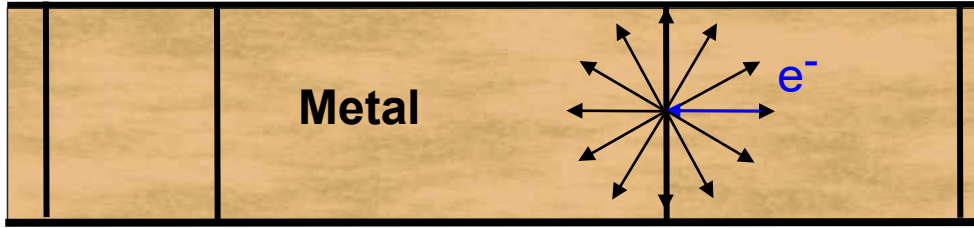


FIG. 2-3 Schematic of electrons incident onto grain boundary assuming interactions with interfaces occur.

However, the more commonly used approach for considering combined surface and grain boundary scattering mechanisms is to assume that surface and grain boundary mechanisms are independent, so Matthiessen's rule can apply. A combined model (FS+MS) for the FS surface, grain boundary, and phonon scattering using this approach can be written as:

$$\rho_{\text{FS+MS}} = \rho_i + \Delta\rho_{\text{FS}} + \Delta\rho_{\text{MS}} \quad (6a)$$

This equation includes the interaction between phonon scattering and surface scattering and the interaction between phonon scattering and grain boundary scattering, but neglects the interaction between grain boundary and surface scattering. In a similar fashion, a combined model (Soffer + MS) for roughness induced surface, grain boundary, and phonon scattering using Matthiessen's rule can be written as

$$\rho_{\text{Soffer+MS}} = \rho_i + \Delta\rho_{\text{Soffer}} + \Delta\rho_{\text{MS}} \quad (6b)$$

and similarly for a combined RK roughness and grain boundary scattering,

$$\rho_{\text{RK+MS}} = \rho_{\text{RK}} + \Delta\rho_{\text{MS}} \quad (6c)$$

FIG. 2-4 is a comparison between the combined FS and MS models using Matthiessen's rule (equation (6a)) and the MSS model described by equation (5) for the hypothetical case of a 30 nm thick film with 30 nm grain size. The interaction between grain boundary and surface scattering is evident in the larger low-temperature resistivity (0.4  $\mu\Omega\text{cm}$ , about 40%, at 10 K) of the MSS model, wherein the scattering of electrons with momentum parallel to the external surfaces by grain boundaries results in additional surface scattering. This interaction is absent in the FS+MS model. At higher temperatures, the scattering of the electrons with momentum parallel to the surfaces is primarily due to phonons in both models and thus negligible resistivity differences are predicted.

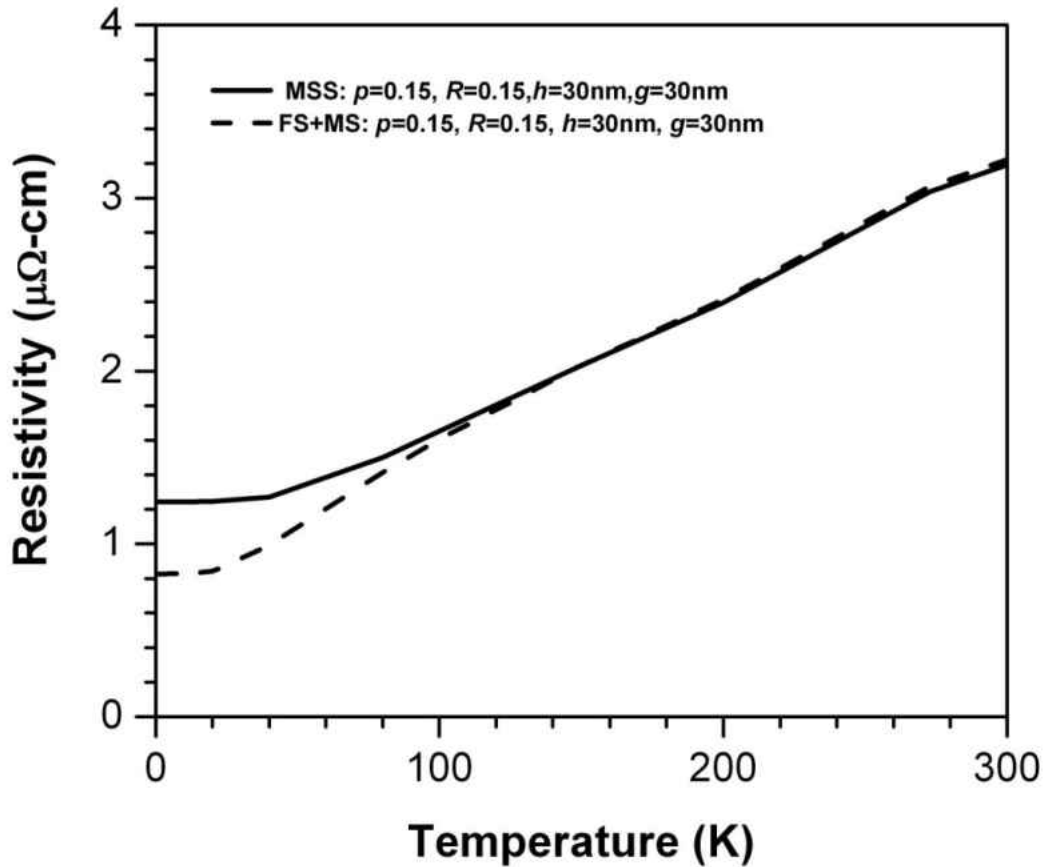


FIG. 2-4. Temperature dependence of the total resistivity of two combined surface and grain boundary scattering models for a Cu thin film with both a thickness,  $h$ , and a grain size,  $g$ , of 30 nm. The MSS model refers to the model described in equation 5 in which interactions between the two additional scattering mechanisms are considered.<sup>15</sup> The FS+MS model refers to the simple Matthiessen's rule combination (equation 6a) of these two scattering effects. For both models the surface specularity parameter,  $p$ , and the grain boundary reflection coefficient,  $R$ , are set equal to 0.15.

Another complication in comparisons between experimental data and the various models is



the choice of an appropriate value for the bulk resistivity of Cu,  $\rho_i$ . Ideally, sufficiently high purity Cu samples should be used, where impurity scattering is negligible, and the bulk room temperature (293 K) value due to phonon scattering can be used,  $\rho_i = 1.67 \mu\Omega\text{cm}$ . However, this value is rarely used and  $\rho_i$  is more often considered an additional free fitting parameter by experimentalists.

## 2.6 Scattering From Impurities and Voids

The presence of impurities and voids can increase the resistance of polycrystalline conductors over and above that from surface and grain boundary scattering. Higher concentrations of impurities, such as Al, O and C, have been observed in thin films and a modest resistivity increase of  $\sim 0.01 \mu\Omega\text{cm}$  has been attributed to impurity scattering in high purity ( $\geq 99.99\%$ ) Cu thin films.<sup>24</sup> Other studies of the classical size effect have reported very substantial contributions to resistivity from impurity scattering, but only rarely have the sample impurity contents been separately measured.<sup>30,31</sup> Voids are also often found in thin films as a by-product of processing, and while typically not of the length scale to affect resistivity directly, voids can result in substantial errors in the measurement of sheet resistance that is used to experimentally calculate resistivity. Characterization of sample void volumes is, unfortunately, also rarely included in experimental reports. While extreme voiding (void area fraction  $> 50\%$ ) can often be observed by visual inspection, intermediate levels of voiding that are not evident without electron microscopies can be a significant part of the resistance increase observed.

## CHAPTER 3

## EXPERIMENTAL LITERATURE REVIEW

### 3.1 Introduction

Most recent experimental studies of the classical size effect include the fitting of resistivity data to the surface scattering model of Fuchs and/or the grain boundary scattering model of Mayadas and Shatzkes<sup>15</sup> for a range of sample thicknesses without detailed microstructural characterization. In this chapter, various experimental approaches to quantitatively measure the relative contribution of scattering mechanisms in nano-conductors and their shortfalls are examined.

### 3.2 Surface Scattering in Single Crystal Metallic Films

Attempts have been made to study surface scattering without the complication of grain boundary scattering by use of epitaxial metallic thin films on single crystal substrates. A common difficulty in the growth of epitaxial films on insulating substrates is the lattice mismatch, which leads to dewetting of the metallic overlayer and an initial or intermediate growth stage of isolated islands and irregular film thickness upon coalescence. An example of this is the growth of Au on mica by Sambles et al.<sup>32</sup> where epitaxial Au films could only be obtained for an intermediate range of thicknesses.<sup>32</sup> Severe porosity was observed for the thinner films, and films thicker than 160 nm were polycrystalline. A more successful example of this approach is the work of Hensel et al.<sup>25</sup> using annealed, lattice matched, epitaxial CoSi<sub>2</sub> films on Si having a thickness range of 6 nm to 110 nm.<sup>25</sup> They concluded that the film resistivity showed little dependence on film thickness,

i.e., that surface scattering was primarily specular. They fitted their low temperature residual resistivity values to the Fuchs surface scattering model and estimated a lower limit to the specular scattering fraction,  $p$ , of 0.9, this value representing an average of the film/substrate and film/air surfaces as shown in FIG. 3-1 . They attributed the increase in resistivity that was observed for their thinnest samples to deterioration in film quality.

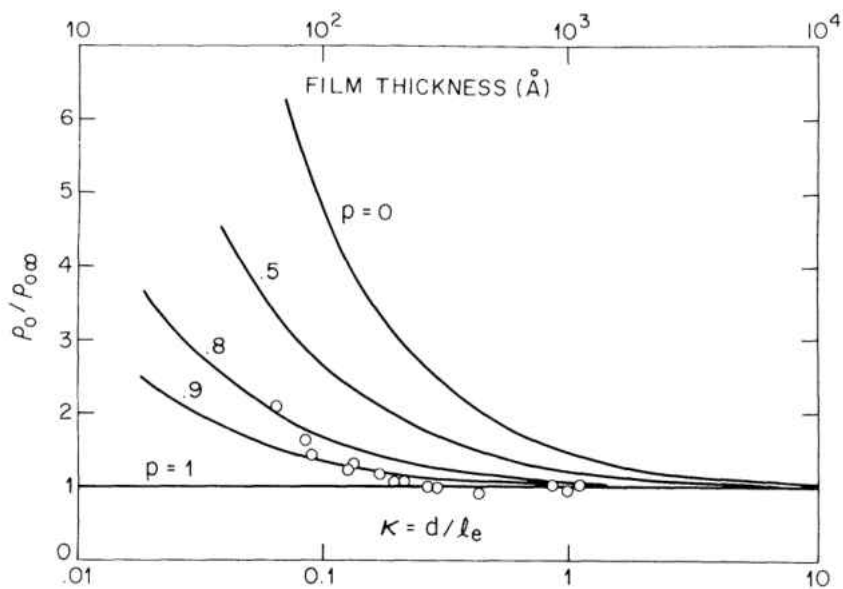


FIG. 3-1. A plot of normalized resistivity as a function normalized thickness. The unfilled circles are experimental resistivity data points of single crystal  $\text{CoSi}_2$  film from Hensel.<sup>25</sup>

Both specular and diffusive scattering have been reported in the technologically interesting metal, Cu. Krastev et al. investigated epitaxial Cu on H-terminated Si(100) samples, and observed a fully diffusive scattering in the samples; however, this might also be due to the impurities and discontinuities present in the samples.

Recently, Chawla and Gall studied epitaxial copper(100) thin film sputter deposited on

MgO(001) at 80 °C and observed partially specular scattering at Cu/Air and Cu/MgO interfaces for films in the range of 20 nm to 1.5  $\mu\text{m}$ <sup>33</sup>. The authors reported a specular coefficient of  $0.6\pm 0.1$  at room temperature and  $0.7\pm 0.1$  for the same set of five samples measured at liquid nitrogen temperature. Microstructural and impurity characterization were not presented in the work, so the homogeneity of the samples is unknown.

### **3.3 Combined Surface and Grain Boundary Scattering in Polycrystalline Metallic Films**

In their initial proposal of a grain boundary scattering mechanism for the classical size effect, Mayadas and Shatzkes<sup>15</sup> assumed equivalence of grain size and film thickness and did not experimentally study the microstructure of their sample. Sambles and colleagues studied the resistivity of single crystal and polycrystalline Au films characterized by X-ray diffraction, scanning electron microscopy and reflection high energy electron diffraction.<sup>32</sup> Experimentally, they were only able to qualitatively (and not quantitatively) describe grain size, and thus, also fit their resistivity data to the MS and Soffer models with assumed thickness dependence to the grain size.

More recently, Attekum et al.<sup>29</sup> studied the temperature dependence of the resistivity size effect in evaporated Au films where they found that the resistivity increase was nearly constant over a wide temperature range. The authors found excellent fit between the temperature dependent resistivity data and the MS model, but found deviations with a Soffer+MS model. It was concluded that grain boundary scattering accounted for the resistivity size effect in their Au thin films, and surface effect was due to a change in the effective Debye temperature.

Lim and colleagues studied Cu films and assumed equivalence of grain size and film thickness. They were able to fit their data to a combined (simple summation) Fuchs and Mayadas model with a surface specular scattering fraction,  $p$ , equal to zero and a grain boundary reflection probability near 0.3.<sup>24</sup> Day et al. were able to provide two different grain sizes at each film thickness by the sputter deposition of Ti films with and without -115V substrate bias.<sup>34</sup> Their grain size was determined by line broadening in X-ray diffraction. Unfortunately, electron microscopy was not used to examine the defect structure of the films, and a thickness dependent room temperature increase in resistivity with ambient atmospheric exposure was reported and presumed to be due to O<sub>2</sub>/H<sub>2</sub>O absorption along grain boundaries. Their resistivity data was fitted to a FS+MS model with  $R = 0.1$  and  $p = 0$ . Harper et al.<sup>35</sup> studied relatively thick (1  $\mu\text{m}$ ) Cu films and used the Mayadas and Shatzkes grain boundary scattering model to describe the resistivity change associated with grain growth (from 0.1  $\mu\text{m}$  to 1.0  $\mu\text{m}$ ) as determined by focused ion beam imaging of the sample. They reported that their experiments were consistent with a grain boundary reflection coefficient,  $R$ , in the range of 0.2 to 0.4. Due to the constant thickness of the films, a Fuchs-like surface scattering component was not examined.

Reports of polycrystalline metal film thickness dependent resistivity, fitted by some combination of Fuchs, Soffer, and Mayadas and Shatzkes scattering models, but without microstructural characterization, are still common in the recent literature.<sup>36,37</sup> Such reports confirm the expected trend of a resistivity increase for thinner films, but do little to extend our scientific understanding beyond the current, mostly qualitative, status.

Whereas the most common sample geometry has been that of a metal film on an insulating substrate, the wire geometry has also been studied, and recent investigations have been motivated

by the importance of the classical size effect to semiconductor interconnect metallurgy. Chen and Gardner were the first to raise this issue.<sup>2</sup> They studied rectangular, annealed, buried Cu wires surrounded by SiN<sub>x</sub> and with a fixed height of 450 nm, and varying widths from 200 nm to 3000 nm. They fitted their resistivity data to the Fuchs model with a surface specular scattering fraction,  $p$ , of 0.47 and noted some deviations from the model that were attributed to grain boundary scattering, but measurements of grain size were not reported. Steinhögl et al.<sup>38</sup> concluded that  $p = 0.6$  and  $R = 0.5$  best fitted their room temperature resistivity data of 230 nm high copper wires with widths ranging from 40 nm to 800 nm, while assuming that the grain size equaled the smallest dimension of the wires. However, the specularity and reflection parameter pairs of  $(p = 0, R = 0.42)$  and  $(p = 1, R = 0.53)$  can fit Steinhögl et al.'s data as well.<sup>30</sup>

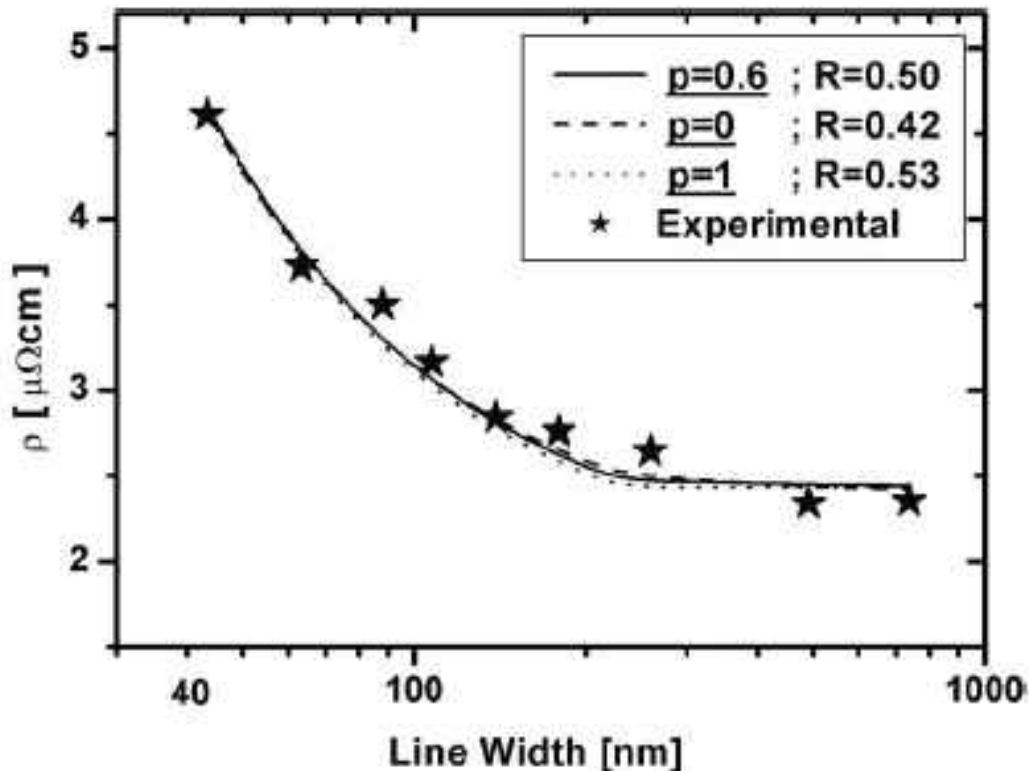


FIG. 3-2. The star shape data points and solid line predicting resistivity increase by FS+MS combined models are from Steinhögl et al.'s work.<sup>38</sup> The dash and dotted lines are resistivity predictions from the FS+MS combined models with different specularly and reflection coefficients plotted by Maroms et al. showing the difficulty of extracting meaningful model parameters by analyzing data without independent variations of grain size and line width.

Marom et al. compared resistivities of Cu thin films to that of Cu wires which were electroplated into SiO<sub>2</sub> trenches with Ta liners.<sup>30</sup> They assumed that the resistivity differences between the Cu wires and films were solely due to additional surface scattering at the sidewalls of the wires while ignoring the grain size differences between the two set of samples. Consequently, fully diffusive scattering was reported in their work.

Very small wires were studied by Durkan and Welland, who fabricated 20 nm thick polycrystalline Au nanowires of widths ranging from 15 nm to 80 nm.<sup>39</sup> In unannealed samples with a 20 nm mean grain size, no size effect was observed, whereas in the annealed samples a size effect was observed. In this latter case, the data was fit to a combined Fuchs and Mayadas model with a surface specular scattering fraction,  $p$ , equal to 0.5 and a grain boundary reflection probability,  $R$ , of 0.9. Bietsch and Michel<sup>40</sup> avoided theoretical description of size effects as “controversial,” but presented data from conducting atomic force microscopy probing along individual nanowires that showed steps in the resistivity that were interpreted as indicative of grain boundaries.

Kitaoka et al. performed electrical measurements of Cu damascene lines using a four-tip STM probe with minimum spacing of 70 nm on a 70 nm wide line.<sup>41</sup> They observed a

resistivity jump approximately every 200nm as the probes were scanned along the line, which corresponded to the average grain size of the line. The resistivity jump due to the encounter of a grain boundary was reported to be 1.2 mΩcm , which they translated into a grain boundary reflection coefficient of 0.64 and a surface scattering specularity coefficient of 0.49.

### 3.4 Approach

To quantify the relative contributions of grain boundary and surface scattering to the classical size effect, the following experimental conditions must be met<sup>17</sup>:

1. The scattering interfaces (for films, the top and bottom surfaces) of the conductor must be identical to avoid uncertainties regarding which interface is quantitatively responsible for the resistivity.
2. The sample set must include independent variation of the conductor's average grain size and of the spacing between exterior surfaces (thickness for films).
3. The structure (e.g., continuity/voiding, thickness, roughness, grain size) of the conductor must be characterized in detail. For grain size, statistically significant populations (typically  $10^3$  grains per sample) must be measured.

The prior discussion showed that no prior experimental study had satisfied these three essential requirements. As a result, there has been much confusion regarding the relative contributions of surface scattering and grain boundary scattering to the classical size effect. In this work, a methodology to control grain size in nano-dimensioned Cu thin films was developed. A definitive quantification of these two contributions to the classical size effect for the technologically important example of copper is presented. The room temperature (296 K, the



typical temperature in the lab) and the liquid He temperature (4.2 K) resistivities of  $\text{SiO}_2/\text{Cu}/\text{SiO}_2$  and  $\text{SiO}_2/\text{Ta}/\text{Cu}/\text{Ta}/\text{SiO}_2$  samples are investigated. The surface scattering is examined in greater detail by considering different resistivity contributions of surface scattering for the two types of interfaces studied, i.e.  $\text{Cu}/\text{SiO}_2$  and  $\text{Cu}/\text{Ta}$ . Further, the impact of the roughnesses of the upper and lower Cu film surfaces on film resistivity is evaluated. The grain size and thickness of the Cu layer of the experimental samples were both varied, and the resistivity data is compared to the various classical size effect models separately to identify the fundamental mechanisms behind the resistivity increase. Further, the room temperature and low temperature resistivity data for both sample types are combined and integrated into the classical size effect models to develop a cohesive description of classical size effect over a wide range of temperature, surface chemical potential, roughness, and grain sizes. Because of these measures, this work is the most complete quantitative measurement of surface scattering in polycrystalline metals in which the resistivity contributions from both the surface and grain boundary scattering have been accurately determined.

## CHAPTER 4                      EXPERIMENTAL PROCEDURES

This work makes use of ultra-high vacuum (process environment and gas purity) sputter deposition to prepare blanket Cu films with thicknesses in the range of 27 nm to 158 nm. The metal films are encapsulated with an underlayer and an overlayer of silicon dioxide to provide similar upper and lower scattering interfaces for the metallic layer. The sputtered films are deposited at sub-ambient temperatures to freeze in an initially non-equilibrium microstructure to promote subsequent grain growth. The films are subsequently annealed in a reducing gas ambient to induce recrystallization and grain growth to produce samples that have reduced resistivity, and to provide a range of grain sizes in order to allow quantification of the classical size effect for these materials. Access to higher temperatures without film agglomeration is made possible by the overlayer encapsulation. Film void fractions and grain size are characterized by scanning transmission electron microscopy (STEM) using high angle annular dark field (HAADF) and by transmission electron microscopy (TEM) using hollow cone dark field imaging (HCDF). X-ray reflectivity is used to measure the thickness of the films. Film resistivity is measured *ex-situ* at 296 K and 4.2 K to vary the electron mean free path and aid extraction of the surface and grain boundary scattering effects.

### 4.1 Sample Preparation

The sample preparation conditions in this work were developed to provide maximum grain size variations for each thickness of the Cu layer for encapsulated structures of SiO<sub>2</sub>/Cu/SiO<sub>2</sub> and

SiO<sub>2</sub>/Ta/Cu/Ta/SiO<sub>2</sub>. Such layered film designs best represent the configurations of working interconnects in integrated circuits, and provide identical top and bottom surfaces for physical modeling of electron scattering at surfaces. Chapter 5 will discuss in detail how the sample processing parameters were determined, and a detailed description of the processing conditions is given in this section.

The encapsulated Cu thin films were prepared on 3” diameter Si (100) substrates having a nominally 150 nm thick layer of thermally grown SiO<sub>2</sub>. The substrates were mounted onto a Cu substrate platen with a mechanical clamp ring and a thin layer of vacuum grease (Apeizon N) between the wafer backside and the platen to insure adequate thermal contact in vacuum. The Cu substrate platen was introduced into a UHV sputter deposition chamber via a load-lock chamber and RF sputter cleaned in 10 mTorr of Ar+2%O<sub>2</sub> for 15 minutes at low power (0.2 W/cm<sup>2</sup>). After cleaning, the substrate and platen were cooled prior to deposition to -40°C by contact with a liquid nitrogen cooled Cu plate. The substrate temperature prior to deposition was controlled by variation of the allowed cooling time and was confirmed for each sample by measurement of plate temperature immediately upon venting. For films having the SiO<sub>2</sub>/Cu/SiO<sub>2</sub> structures, an underlayer of 20 nm of SiO<sub>2</sub> was RF sputter deposited prior to the Cu film deposition and a second 20 nm SiO<sub>2</sub> overlayer was similarly deposited immediately following the Cu layer deposition. For films having the SiO<sub>2</sub>/Ta/Cu/Ta/SiO<sub>2</sub> structure, a layer of 2 nm of Ta was DC sputter deposited immediately prior to, and again after, the Cu layer deposition. These films were otherwise prepared similarly to the SiO<sub>2</sub>/Cu/SiO<sub>2</sub> process described above. The Cu films, of thickness ranging from 27 nm to 158 nm, were deposited by DC sputter deposition from high purity (99.9999%) Cu targets at a rate of 0.6 nm/sec onto the electrically grounded substrates. The SiO<sub>2</sub>

layer depositions were performed at a total pressure of 4 mTorr of Ar process gas while the metal layers were deposited at 2 mTorr of Ar+3%H<sub>2</sub>. A deposition chamber pressure in the 10<sup>-9</sup> Torr range was obtained prior to film deposition and the nominally 99.999% purity Ar was passed through a hot reactive metal getter purifier (SAES Pure Gas) prior to introduction to the chamber.

Annealing treatments of 150°C and 600°C for 30 minutes were performed on both SiO<sub>2</sub>/Cu/SiO<sub>2</sub> and SiO<sub>2</sub>/Ta/Cu/Ta/SiO<sub>2</sub> structure samples in a tube furnace to provide grain size variations at each thickness of the Cu layer. A rapid thermal annealing treatment of 400 °C for 6 seconds was used for two SiO<sub>2</sub>/Cu/SiO<sub>2</sub> samples as a comparative experiment in minimizing film dewetting. An Ar+5%H<sub>2</sub> reducing process gas was used in both annealing treatments to prevent oxidation of the Cu layer. While many samples were prepared over the course of this work, the samples that have been most extensively characterized are summarized in Table 1.

## **4.2 Transmission Electron Microscopy Characterization**

Samples for TEM characterization were prepared by using a back-etch technique, thinning initially with HF + HNO<sub>3</sub> solution to remove the Si wafer substrate and subsequently using a diluted HF solution to obtain a pure Cu film. The microscopy was performed in a Tecnai F30 microscope operating at 300kV.

Table 1 Annealing temperature, thickness, root mean square roughnesses (upper,  $r_1$ , and lower,  $r_2$ , of the Cu/encapsulant layer interfaces), 296 K and 4.2 K resistivity, and grain size data for  $\text{SiO}_2$ -encapsulated Cu thin films (Table 1a), and the Ta/ $\text{SiO}_2$ -encapsulated Cu thin film (Table 1b).

Table 1a $\text{SiO}_2/\text{Cu}/\text{SiO}_2$								
Anneal (°C)	Voiding (%)	Thickness (nm)	$r_1$ (nm)	$r_2$ (nm)	$\rho$ @ 296 K ( $\mu\Omega\text{cm}$ )	$\rho$ @ 4.2 K ( $\mu\Omega\text{cm}$ )	Grain dia. (nm)	Grains Measured
150	0.2	27.0	1.2	0.8	3.99±0.20	2.04±0.10	40.5±2.5	483
150	0.1	31.6	1.4	0.8	3.63±0.16	1.62±0.08	47.7±2.8	525
150	0.1	35.3	1.1	1.0	3.20±0.16	1.3±0.07	54.3±2.1	1363
150	1.3	37.1	0.9	0.8	3.08±0.15	1.14±0.06	64.8±2.5	1,362
150	0.0	45.1	1.0	0.8	2.75±0.14	0.9±0.06	101.1±4.6	919
150	0.0	71.8	0.6	1.5	2.30±0.12	0.52±0.03	171.7±7.9	872
150	0.2	136.7	1.2	2.0	2.06±0.10	0.27±0.01	342.2±20.1	525
150	0.0	143.9	0.9	1.3	2.01±0.10	0.25±0.01	248.0±17.2	412
400	2.1	41.7	1.0	0.7	3.05±0.15	0.95±0.05	87.7±3.2	1,563
400	1.4	83.6	0.6	1.1	2.25±0.11	0.36±0.02	221.5±10.7	785
400	0.0	157.9	0.5	2.0	1.92±0.10	0.19±0.01	419.3±21.8	662
600	2.4	33.6	0.2	0.7	2.94±0.15	0.92±0.05	68.4±4.4	452
600	1.9	36.9	0.5	1.0	2.70±0.14	0.78±0.04	81.4±4.5	576
600	1.5	46.4	0.4	0.9	2.54±0.13	0.58±0.03	112.6±7.7	419
600	0.9	74.5	0.3	1.0	2.25±0.11	0.34±0.02	220.0±9.5	1045
600	0.6	149.7	0.3	1.2	1.94±0.10	0.16±0.01	425.2±15.7	1520
Table 1b $\text{SiO}_2/\text{Ta}/\text{Cu}/\text{Ta}/\text{SiO}_2$								
Anneal (°C)	Voiding (%)	Thickness (nm)	$r_1$ (nm)	$r_2$ (nm)	$\rho$ @ 296 K ( $\mu\Omega\text{cm}$ )	$\rho$ @ 4.2 K ( $\mu\Omega\text{cm}$ )	Grain dia. (nm)	Grains Measured
600	0.0	28.3	0.8	1.1	0.2±0.20	1.82±0.09	34.6±1.5	960
600	0.0	34.2	1.1	1.2	3.73±0.19	1.76±0.09	39.4±1.7	1020
600	0.0	38.7	1.3	1.3	3.69±0.18	1.68±0.08	44.3±2.2	743
600	0.0	48.4	1.0	1.0	2.95±0.15	0.99±0.05	69.6±3.4	776
600	0.0	77.9	1.4	1.2	2.55±0.13	0.68±0.03	110.1±4.6	1129
600	0.0	153.1	0.9	1.5	2.08±0.10	0.32±0.02	345.1±15	1033

### 4.2.1 Void Fraction Measurement

The TEM samples were examined by high angle annular dark field (HAADF) imaging in STEM mode at relatively low magnifications to assess the fraction of voids present in the film. The HAADF imaging mode is sensitive to atomic number contrast and provides very strong image contrast for voids. Surface diffusion of Cu atoms can result in the formation of voids (holes) in the film and the redistribution of the Cu atoms to increase the local thickness of the films. At low void area fractions (<5%) this redistribution of Cu does not reduce the cross-sectional area of thin film available for in-plane conduction, and can be considered to have a negligible effect on film resistivity. At high void fractions, the sample resistivity is increased, as the intersection of voids leaves portions of the Cu volume of the sample unavailable to contribute to conduction.

The void fraction was calculated from the HAADF imaged as the simple ratio of dark to the total number of pixels (dark + grey) present in a series of images. This void area quantification technique was also used to guide the development of the deposition and processing techniques described above. The void fractions of the 22 primary samples (for which further characterization was conducted, e.g., grain size, electrical resistivity) are summarized in Table 1 and were found to be between 0 and 2.4%. The resistivity errors that these void area fractions can give rise to are described in the Appendix A and correspond to negligibly small error (i.e., a 0.4% resistance error for the case of a 2.4% void area fraction). FIG. 4-2 is a pair of HAADF images of the 136.7 nm thick sample annealed at 150°C, wherein the voids are identifiable as dark regions in the left-hand image and false color (green) is used to indicate the void pixels in the right-hand image. The void fraction was calculated as the ratio of dark pixels to the total number of pixels (dark + grey) present in a series of images. The void area fraction of the 136.7 nm

$\text{SiO}_2/\text{Cu}/\text{SiO}_2$  sample annealed at  $150^\circ\text{C}$  shown in FIG. 4-1 is determined to be 0.2%.

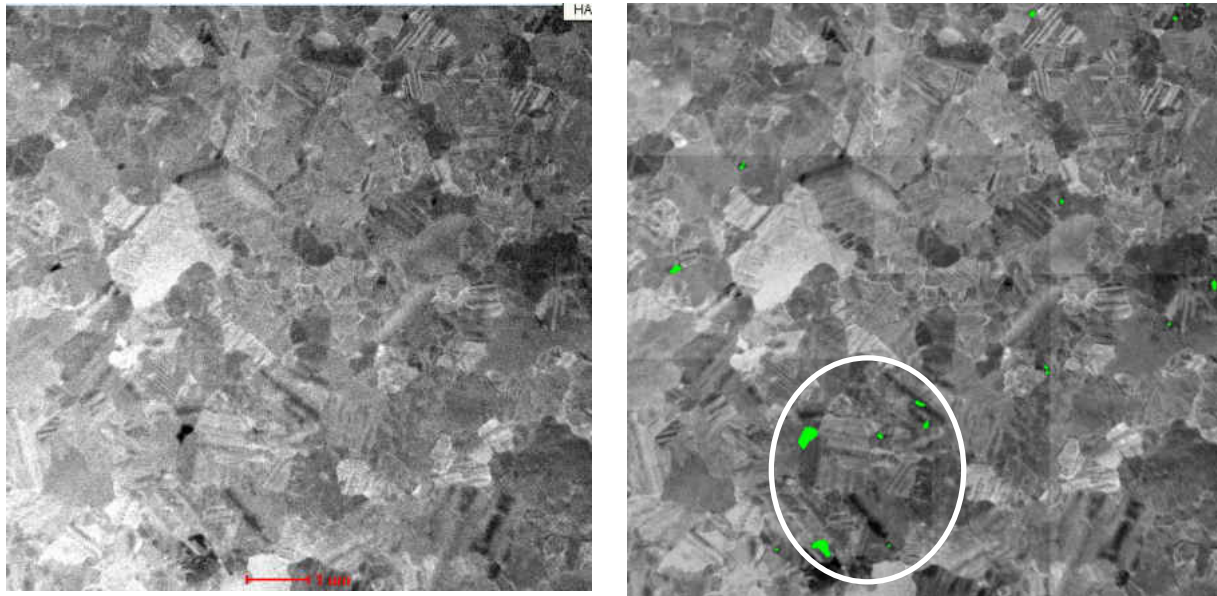


FIG. 4-1. Determination of void fraction in a field of view in 136.7nm  $\text{SiO}_2/\text{Cu}/\text{SiO}_2$  sample annealed at  $150^\circ\text{C}$ , the void area fraction is 0.2 %

#### 4.2.2 Grain Size Measurement

The TEM samples of both the  $\text{SiO}_2/\text{Cu}/\text{SiO}_2$  and  $\text{SiO}_2/\text{Ta}/\text{Cu}/\text{Ta}/\text{SiO}_2$  film structures were examined by hollow cone dark field (HCDF) imaging in TEM mode to provide the highest diffraction contrast for grain size measurements. Multiple images of each field of view were acquired at different sample tilts to provide an enhanced diffraction contrast. Enlarged prints were made of each of the HCDF TEM images taken at different tilts for a given field of view for a given sample. All grain boundaries in the tilt series were hand-traced onto transparency sheets using a fine point permanent marker. The twin boundaries within grains were excluded as twin

boundaries were reported to contribute little on sample resistivity.<sup>42</sup> This hand tracing is necessary because the complex contrast in TEM images, including HCDF images, precludes the use of automated image analysis methods.

Once all the discernable boundaries from all the images in the tilt series were traced, the transparency was overlaid on the image taken at zero sample tilt to recheck the tracing. Grains for which the tracing of boundaries was uncertain were excluded from the measurement.

For very thin samples, in the range of 27 nm to 48 nm, the grain size appeared more uniform and there were few bend and strain contours, resulting in more uniform contrast within grains. The twin boundaries were easy to identify, because they would terminate at the grain boundaries. Further, few grain overlaps were identified, resulting in tracings with a high degree of confidence. An example of the microstructure characteristic of the 41.7 nm film annealed at 400 °C is shown in FIG. 4-2.



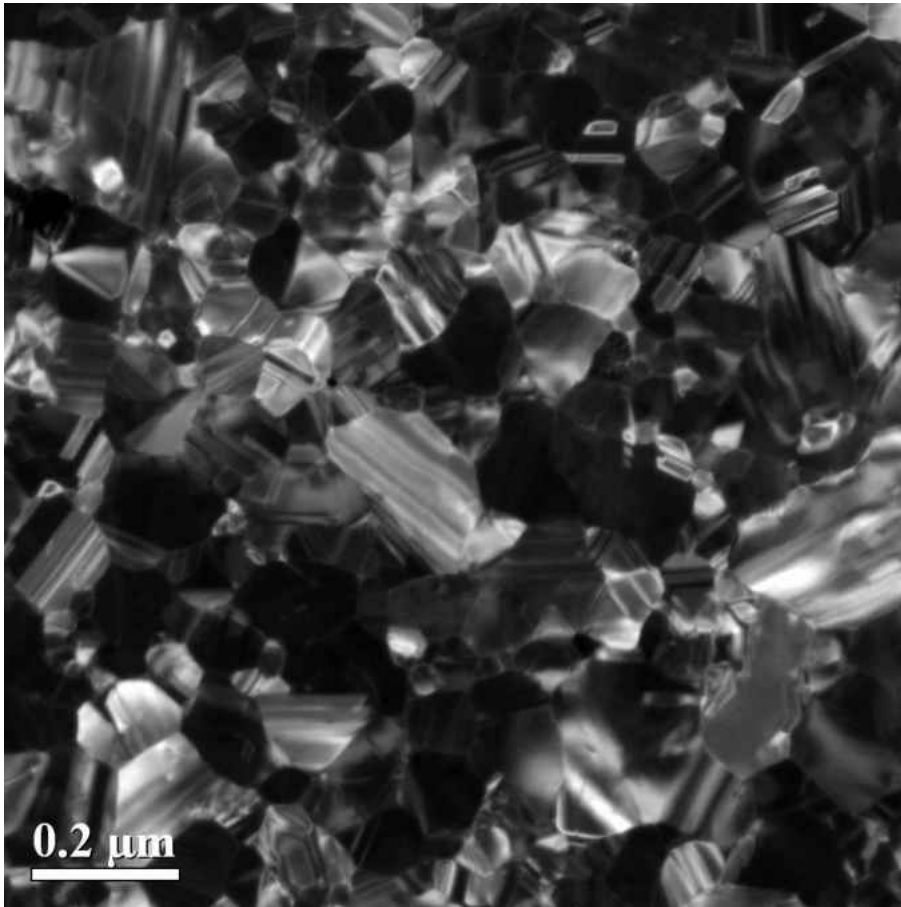


FIG. 4-2. HCDF image of the 41.7 nm sample annealed at 400°C.

For the intermediate thick films, in the range of 71.8 nm to 83.6 nm, the grains appeared less uniform in size, with large grains adjacent to clusters of small grains. Because of the more diffuse contrast within the clusters, possibly as a result of through-thickness grain overlaps, boundaries were more difficult to trace in these regions. Conversely, the boundaries of large grains were sharper and could be traced with greater confidence. However, larger grains also had a higher chance of being edge grains that are not included in the measurements. Overall, the confidence level in the tracings for the intermediate thick films is less than that for the very thin films. An

example of the microstructure of the 83.6 nm thick films is shown in figure FIG. 4-3, as HCDF images of two tilts of the same field of view, wherein a region of grain overlap is identified.

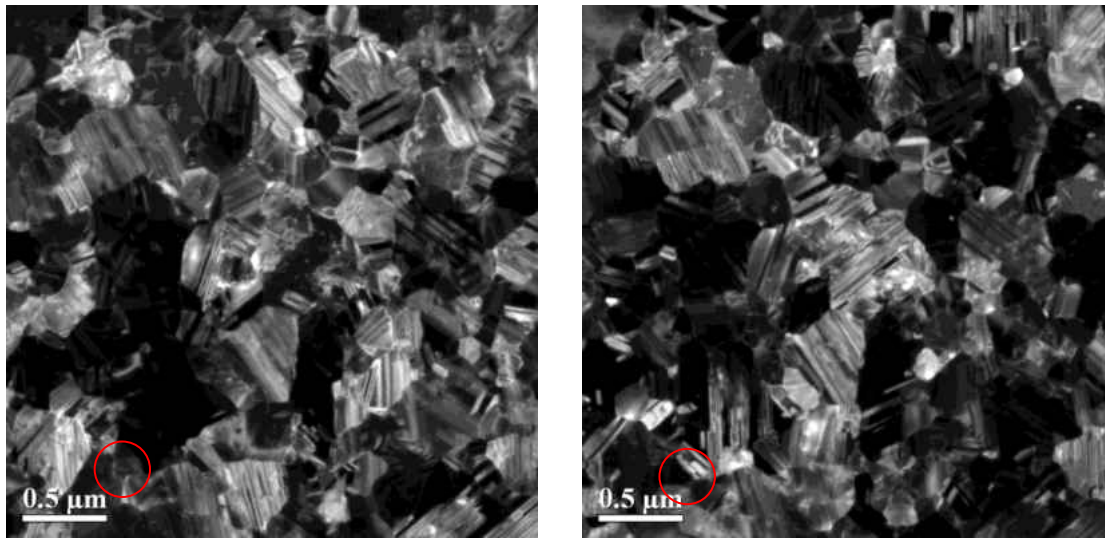


FIG. 4-3. HCDF images at different tilts of one field of view of an 80 nm sample annealed at 400°C. The red circles indicate a region of grain overlap.

The very thick films, with thickness ranging from 136.7 nm to 157.9 nm, show bundles of dislocation lines within the grains, indicating that these films have higher defect content than the two thinner films. The contrast of the dislocation clusters is at times similar to that for grain boundaries, making the tracing of boundaries difficult. As a result of these additional defects within grain interiors, the tracings for these films are the least certain. An example of the microstructure for the 157.9 nm sample annealed at 400°C is shown in figure FIG. 4-4.

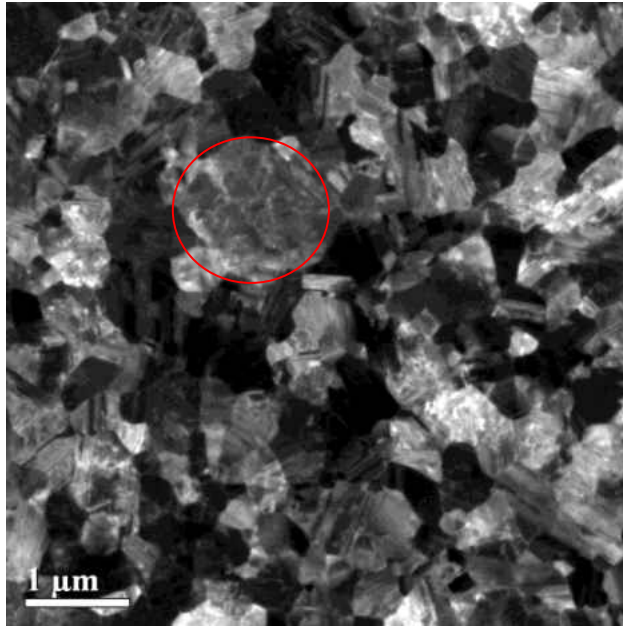


FIG. 4-4. HCDF image of a 157.9 nm sample annealed at 400°C. The red circles indicate a region of dislocations.

The black-on-clear transparencies of traced grain boundaries were analyzed using Image J,<sup>43</sup> an automated image analysis software. To account for the finite width of grain boundaries, both grain area and perimeter were measured. Half of the area associated with the grain boundary was added to the grain area. The reported grain size is the diameter of the equivalent circle with area equal to the mean grain area:

$$\text{Grain size} = \sqrt{\frac{4 \times (\text{mean grain area})}{\pi}} .$$

The errors on the mean grain sizes are determined from the number of grains counted, assuming the grain size distribution to be lognormal. These errors are quoted as  $2\sigma$  values at a 95% confidence level for the given grain population of each sample in Table 1.<sup>44</sup>

### 4.3 X-Ray Reflectivity Characterization

X-ray reflectivity is a powerful technique for the study of surfaces and buried interfaces in thin film systems.<sup>45, 46, 47, 48, 49</sup> In specular x-ray reflectivity, a narrow beam of x-rays is incident upon a specimen and the intensity of the beam reflected at an angle equal to the incident angle is measured. The variation of reflected beam intensity as a function of the common incidence and reflection angle contains information regarding sample density, sample thickness, and root mean square roughness (RMS roughness). In this work, Cu layer thickness and the RMS roughness of the interfaces between the Cu layer and the immediately adjacent layers (either SiO<sub>2</sub> or Ta) were studied by performing both a specular geometry scan and an off-specular geometry scan on the thin-film diffraction beam line 2-1 at the Stanford Synchrotron Radiation Lightsource. The off specular scan ( $\omega=2\theta/2 \pm 0.15^\circ$ ) was subtracted from the specular scan ( $\omega=2\theta/2 = \theta$ ) to acquire a purely specular reflectivity pattern. The beam line is equipped with a Huber 2-circle goniometer, a pair of 1 mm slits as the analyzer<sup>50</sup>, and a He filled sample stage was used to decrease the air scattering background. X-rays with a wavelength of 1.549 Å were monochromated with a double bounce Si(111) crystal. Data were collected for  $2\theta$  values ranging between 0.2° to 12°, with a step size of 0.02°, 0.01°, or 0.005°, depending on film thickness. The X-ray data was analyzed using Bede REFS software as shown in FIG. 4-5. The periods of the Fresnel oscillations correspond to the thickness information of the thin film layers, and the decay of the reflection intensity is due to films' interfaces roughness.

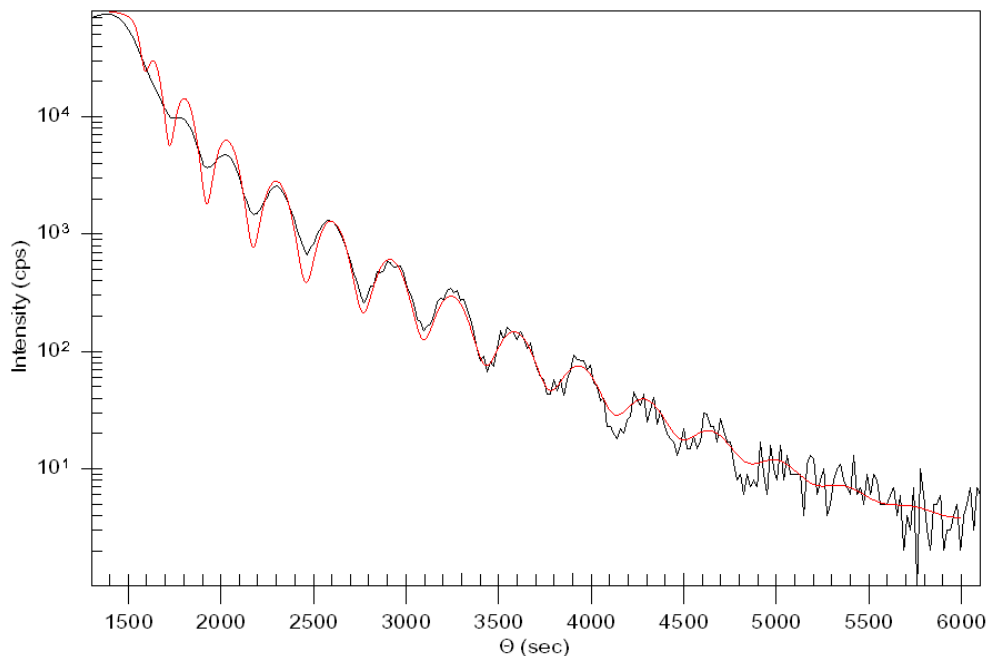


FIG. 4-5 Comparison of XRR data and fit (red curve) for the 41.7 nm thick Cu film annealed at 400°C.

#### 4.4 Cu Thin Film Festivity Measurement

The sheet resistance of the annealed samples was measured by manually placing contact pins onto a square sample coupon using the Van der Pauw geometry<sup>51</sup> on a dipping probe fixture, as shown in FIG. 4-6. The error of the Van der Paul is generally within 3% and sources of errors include contact size, sample symmetry, and thermoelectric effect.<sup>51</sup> The system used a coupled Keithley 2400 Source meter and 2182 nanovoltmeter with a reversing polarity square wave current signal to determine the sample resistance independent of thermal voltages that may have been present. The room temperature sheet resistance was measured in a climate-controlled laboratory environment at 296K, while the 4.2 K resistance of the samples was measured after mounting onto

the dipping probe and immersion of the sample in liquid He to insure a 4.2K sample temperature. Both the 296K and the 4.2 K resistivities presented in Table 1 were determined by multiplying the measured sheet resistance with film thickness determined from the X-ray reflectivity measurement. The combined error of the resistivity of each samples is estimated to be within 5% with less than 3% error from the sheet resistance measurement and less than 3% error from the X-ray thickness measurement. The resistivities observed in this work are lower than that typically achieved for films deposited at a similar thicknesses, and are closer to the resistivities reported for large grained (several micron) films of similar thickness prepared by epitaxy, or mechanical thinning of an initially thicker film.<sup>4,52</sup>

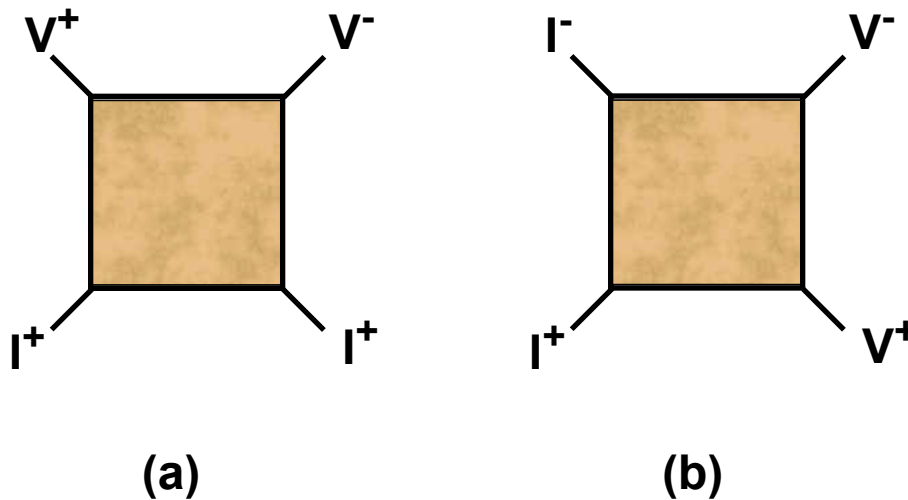


FIG. 4-6. Configuration of the Van der Pauw geometry dipping probe

#### 4.5 Secondary Ion Mass Spectroscopy Characterization

Compositional profiling with secondary ion mass spectrometry (SIMS) was used to

examine Cu film purity The analysis was performed in a Cameca IMS-3F SIMS ion microscope with a 1 $\mu$ m lateral resolution, 8nm depth resolution, and 200 to 10000 mass resolution. Both an O<sub>2</sub> beam for metal detection and a Cs beam for non-metal detection were used in SIMS characterization of the samples. The major impurity observed in the Cu layer was oxygen, which was found to have an upper bound of 30 ppm, but a lower limit could not be established because of the persistence of an oxygen signal from the encapsulation layer throughout the Cu layer.

## **CHAPTER 5                      CONTROLLING GRAIN SIZE IN ENCAPSULATED CU THIN FILMS**

As discussed in previous chapters, systematic independent variation of grain size and film thickness is the key to evaluating the relative contributions of grain boundary scattering and surface scattering to the film resistivity quantitatively. The minimum grain size desired for this study was that equal to the film thickness, to avoid overlapping grains when measuring grain size in the plan-view TEM images, and this was readily achieved by low temperature annealing. There was no upper limit to the desired in-plane grain size at any thickness, but de-wetting and excessive void formation would occur during annealing at higher temperatures to induce grain growth. Thus, the ability to obtain a set of samples with independent variation of thickness and grain size became an experimental problem to maximize grain growth while minimizing void formation. The inherent difficulty lies in the fact that grain growth stagnates when grain size of the film reaches a value comparable to the thickness of the film.<sup>15</sup> Such stagnation is often referred to as specimen thickness effect and has been attributed to a combination of mechanisms: a reduction in the driving forces for grain growth, solute precipitation, and grain boundary grooving at the upper and/or lower interfaces.<sup>53</sup> To control grain size in thin films, optimum substrate preparation and deposition parameters, film structures, and post-deposition annealing parameters were explored.



## 5.1 Pre-Deposition Plasma Etch

For thinner films, the primary experimental difficulty has been to obtain and maintain a continuous film. Small particles and chemically inhomogeneous spots on a wafer can often act as nucleation sites during void formation and can also pin grain boundaries during grain growth. Cleaning the wafers by a plasma etch process at low energy before deposition is an effective process to produce a microscopically clean surface<sup>54</sup> as the bombardment of the ions will remove particles and chemical inhomogeneities on substrate surfaces. However, if the power of the etching plasma is too high, or the pressure of the background is too low, the bombardment ions may be implanted into the substrate surface, and act as nucleation sites.

In an effort to determine optimal pre-etching process conditions, 10 mT of an Ar+3%H<sub>2</sub> reducing gas was compared with that of an Ar+2%O<sub>2</sub> during a pre-etch of 40 nm-thick Cu films encapsulated in Al<sub>2</sub>O<sub>3</sub>. FIG. 5-1 compares examples of HAADF transmission electron micrographs of 800°C annealed 40 nm-thick Cu films encapsulated in Al<sub>2</sub>O<sub>3</sub>, where the substrates were plasma etched before deposition: under a reducing gas of Ar+3%H<sub>2</sub> as in (a), and under a oxidation gas of Ar+2%O<sub>2</sub> as in b). The voids in the figure are identified by the light region. The fraction of voids in the sample pretreated with Ar+2%O<sub>2</sub> was less than the sample pretreated with Ar+3%H<sub>2</sub>. The high reactivity of the oxidizing gas appeared to be more effective in removing surface contaminants than that of the reducing gas.

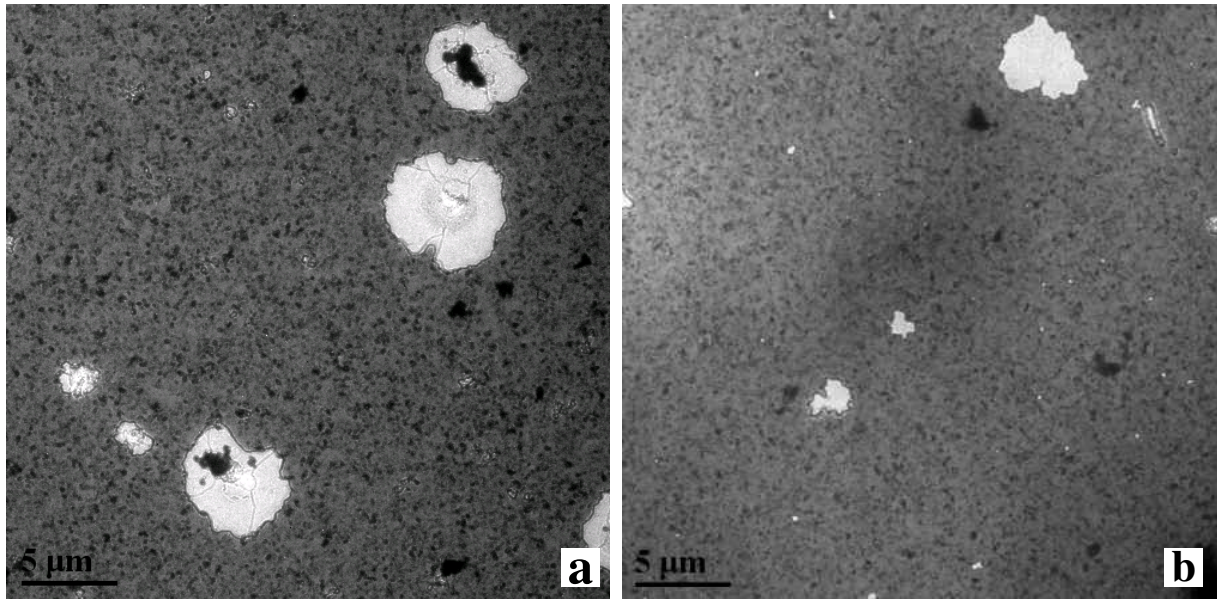


FIG. 5-1. HAADF transmission electron micrographs of 800°C annealed (30 minutes) 40 nm-thick Cu films encapsulated in  $\text{Al}_2\text{O}_3$  with Si/SiO<sub>2</sub> substrate pre-etched by a) Ar+3%H<sub>2</sub> and b) Ar+2%O<sub>2</sub> gas in a biased 30W plasma.

## 5.2 Deposition Conditions

The substrate temperature during deposition is an important parameter in controlling film texture and grain size.<sup>55</sup> The energy released by a grain boundary is estimated to be  $3\gamma_B/g$ , where  $\gamma_B$  is the grain boundary energy and  $g$  is the grain size. Consequently, 1.5 MJ/m<sup>3</sup> or 1.1 meV/atom of energy will be released during the process of a 100 nm diameter grain growing into a 1000 nm diameter grain. Depositing thin films at cryogenic temperature often results in a sample having initially smaller grains and a greater defect density. The higher initial density of grain boundaries and defects was hypothesized to provide an increased driving force for grain growth during annealing (as in recrystallization) and hence result in a film with larger average grain size after annealing. It was also hypothesized that the lower deposition temperature would provide for a Cu

film having an upper surface that was more conformal to the lower (substrate) interface. The topography of this upper Cu surface would then be followed by the subsequent deposition of the encapsulation layers (SiO<sub>2</sub> or Ta/SiO<sub>2</sub>) interface. As asperities in this interface were considered to have the potential to pin grain boundaries during annealing, this is also a mechanism by which low temperature deposition might allow a subsequently enhanced grain growth.

While the full understanding of the mechanisms is not clear, the low temperature deposition was observed to significantly aid in obtaining large grain sizes within the annealing limitation of minimal void area formation. FIG. 5-2 gives the bright-field transmission electron micrographs of 800°C annealed Al<sub>2</sub>O<sub>3</sub>/Cu/Al<sub>2</sub>O<sub>3</sub> samples deposited at a) -40 °C, and b) -120°C. The Cu layer and Al<sub>2</sub>O<sub>3</sub> layers are 40 nm and 20 nm thick respectively. The average grain size of the Al<sub>2</sub>O<sub>3</sub>/Cu/Al<sub>2</sub>O<sub>3</sub> sample deposited at -120°C grows from 35nm to 135nm after annealed in tube furnace at 800°C for 30 min, and clearly has a larger average grain size than the annealed sample deposited at -40 °C.

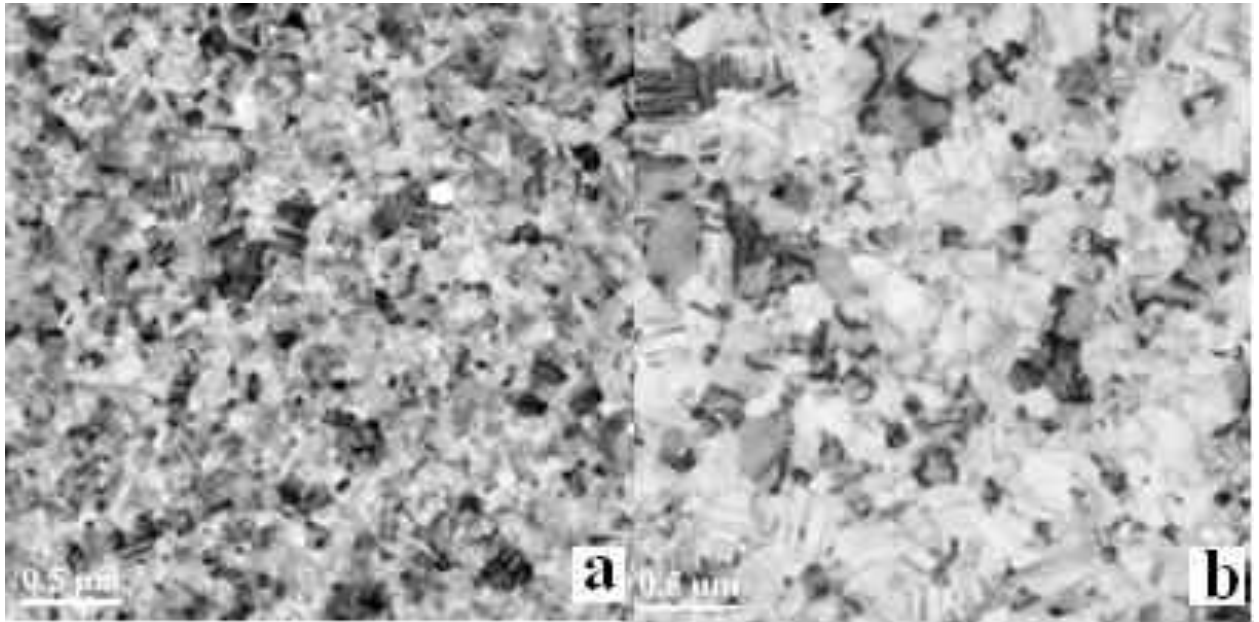


FIG. 5-2. Bright-field transmission electron micrographs of 800°C annealed  $\text{Al}_2\text{O}_3/\text{Cu}/\text{Al}_2\text{O}_3$  deposited at a) -40 °C, and b) -120°C.

The Ar + H<sub>2</sub> processing gas pressure during deposition also has an effect on the final microstructure of the annealed films. FIG. 5-3 shows the bright-field transmission electron micrographs of 800°C annealed 40 nm thick Cu films encapsulated with 20 nm of Al<sub>2</sub>O<sub>3</sub> sputter deposited in plasma with 2 mT(a), 8 mT (b), and 16 mT (c) of Ar+3%H<sub>2</sub>, where the deposition times were varied (58 seconds, 75 seconds, and 109 seconds, respectively) to allow a constant deposition power to be used and to produce films of same thickness (high processing gas pressure during sputtering slows down deposition rate).<sup>54</sup> The lower gas pressure (2 mT) appears to have favored a more continuous film structure (fewer voids) and has larger grains after annealing.

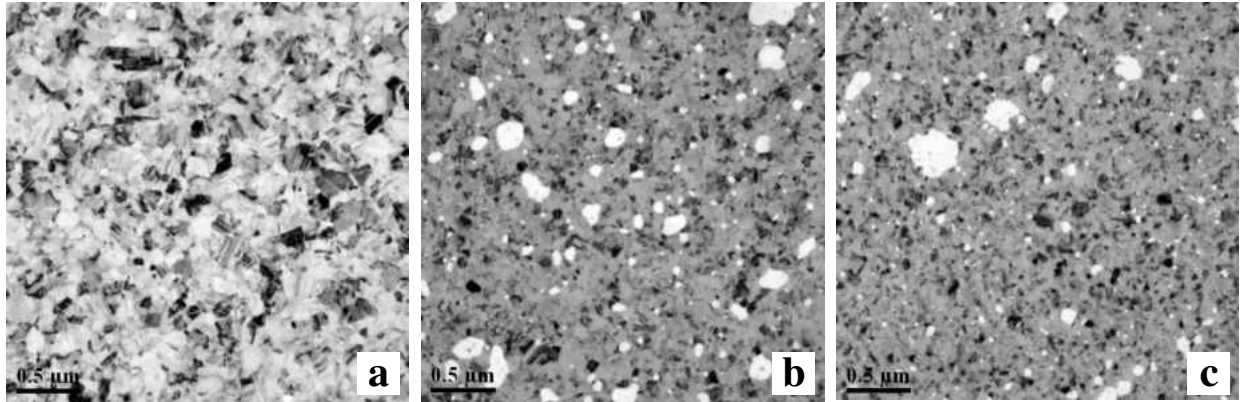


FIG. 5-3. Bright-field transmission electron micrograph of 800°C annealed 40 nm thick Cu film encapsulated with 20 nm of Al<sub>2</sub>O<sub>3</sub> deposited (a) in 2mT Ar+3%H<sub>2</sub> (b) 8mT Ar+3%H<sub>2</sub> (c) 16mT Ar+3%H<sub>2</sub>

### 5.3 Energized Particle Bombardment

Low energy Ar ion bombardment during deposition has been known to be effective for microstructural modification and promote grain growth. Nita et al. has reported observations of ~10X grain size after annealing 1 μm thick copper films which had undergone particle bombardment during deposition.<sup>56</sup> The lower process gas pressure (2mT) studied above is known to allow greater bombardment of the growing film by energetic ions and neutrals from the target surface. Energetic bombardment was further explored by the deposition of Al<sub>2</sub>O<sub>3</sub>/Cu/Al<sub>2</sub>O<sub>3</sub> samples in 2 mT Ar+3%H<sub>2</sub> with RF substrate bias powers of 0W, 5W, 10W, and 30W to provide a further increase in the bombardment of the developing films with Ar and H ions during deposition. It was found that, contrary to our expectation, the grain size of annealed samples with bias was smaller than samples deposited without bias, as shown in FIG. 5-4. It appears excessive bombardment is undesirable, possibly because Ar and H ions were implanted into the Cu film and caused impurity pinning of grain boundaries during grain growth.<sup>57</sup>

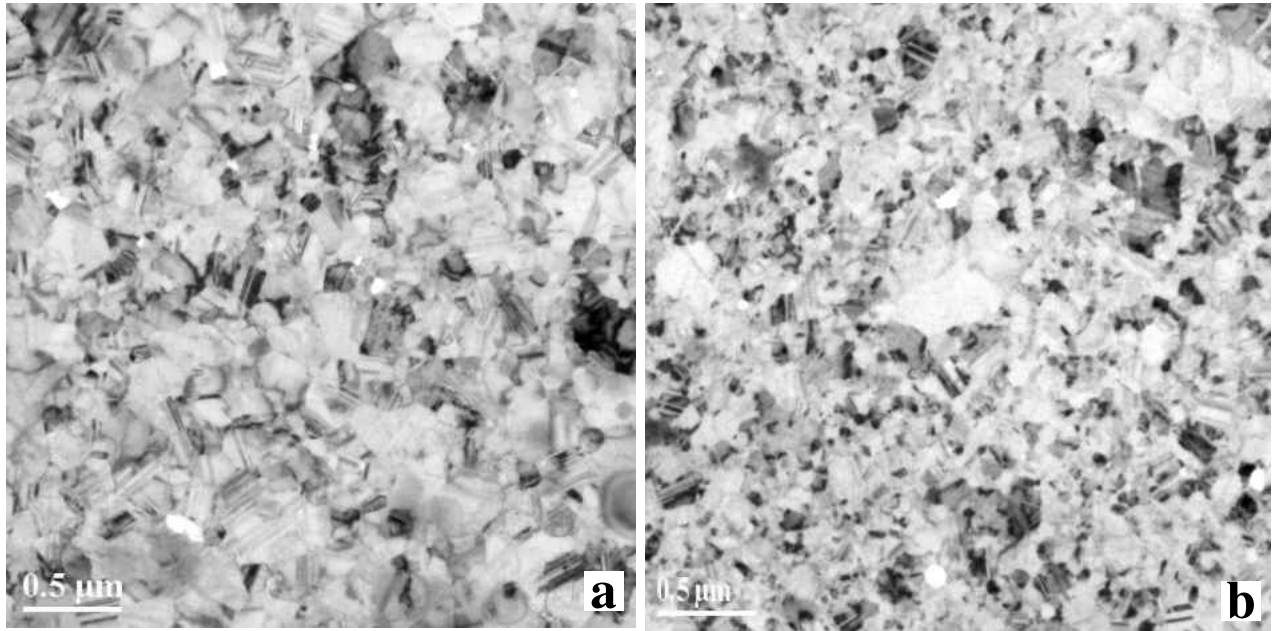


FIG. 5-4. Bright-field transmission electron micrograph of 800°C annealed 40 nm thick Cu film encapsulated with 20 nm of Al<sub>2</sub>O<sub>3</sub> deposited (a) without bias and (b) with 30 W bias.

#### 5.4 Annealing Parameters

The choice of the annealing ambient gas has a profound effect on the microstructure of the films, as the use of a reducing gas can prevent the formation of oxides. Oxides may pin grain boundaries and acts as nucleation sites for void formations in thin films.<sup>53</sup> In FIG. 5-5, the 20 nm Cu film encapsulated in Al<sub>2</sub>O<sub>3</sub> was annealed in Ar+3%H<sub>2</sub> and showed better continuity than that the 20 nm Cu film annealed in a non-reducing gas.

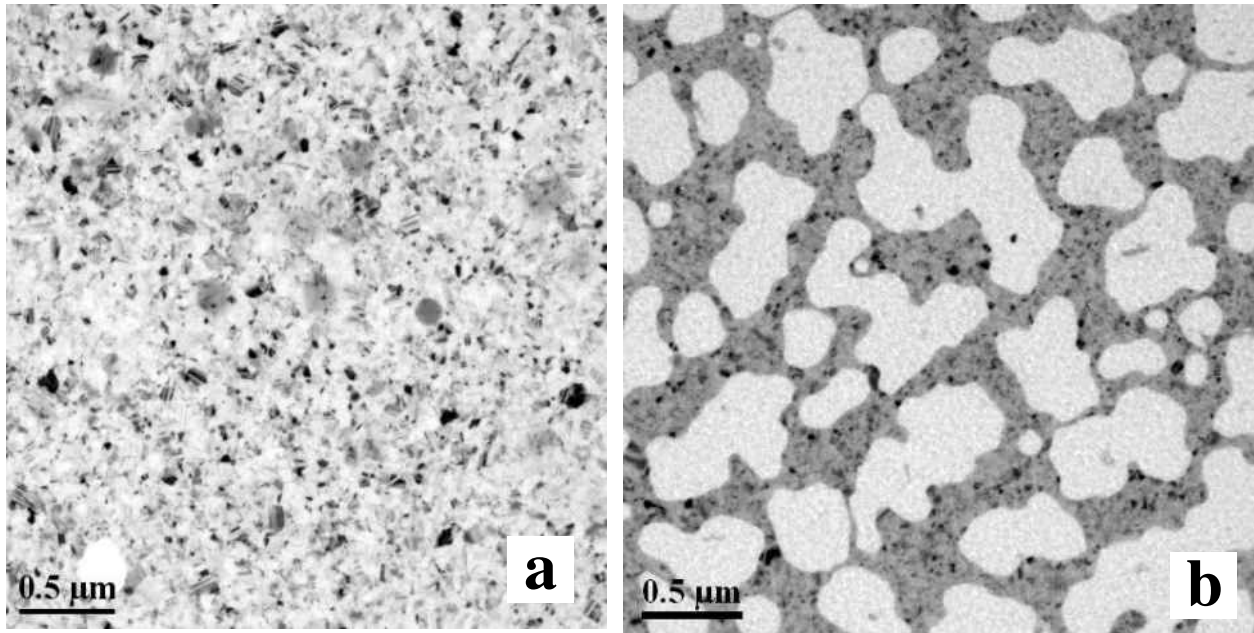


FIG. 5-5. Bright-field transmission electron micrograph of 400 °C annealed 20 nm Cu film encapsulated in Al<sub>2</sub>O<sub>3</sub> (a) annealed in a reducing gas of Ar+3%H<sub>2</sub>, (b) in a non-reducing gas, for 40 minutes .

While increased annealing temperature is well understood to promote grain growth, high annealing temperatures also promote void formation. Three encapsulant materials, Al<sub>2</sub>O<sub>3</sub>, SiO<sub>2</sub>, and Si<sub>3</sub>N<sub>4</sub>, were studied to identify the preferred material for this compromise between grain growth and void formation.<sup>58</sup> This effort is summarized in Table 2, which presents the grain size of 40 nm-thick Cu films encapsulated in 20 nm-thick layers of these three dielectric encapsulation materials. The grain size of films annealed at 800°C is on average 50% larger than films annealed at 400°C. From the table it appears that Al<sub>2</sub>O<sub>3</sub> is preferred. However this encapsulant material often provided poor contrast for the HCDF imaging and accordingly was not used. The SiO<sub>2</sub> encapsulant was chosen for the primary samples reported in table 1.

It was also observed that the trend of greater grain growth with increasing anneal temperature breaks down beyond 800°C. As shown in FIG. 5-6, the microstructure and grain size of Al<sub>2</sub>O<sub>3</sub>/Cu/ Al<sub>2</sub>O<sub>3</sub> sample annealed at 800°C are similar to the 1000°C annealed samples, but with more voids. This stagnation in grain growth is presumed due to the ability of voids to pin grain boundaries during annealing. To insure a low void fraction for even the thinner films, an upper anneal temperature of 600°C was chosen for most of the primary film samples. The lowest annealing temperature of 150°C was chosen to insure that no significant room temperature grain growth occurred during the post-deposition characterization of the films, which spanned a period of several months for many of the samples.

Table 2. Grain size and void area fraction of 40 nm-thick Cu films encapsulated in 20 nm-thick films of four dielectric encapsulation materials. The films were annealed at 400°C or 800°C.

<b>Dielectric Encapsulant</b>	<b>Annealing Temperature (°C)</b>	<b>Grain Size (nm)</b>	<b>Void Fraction (%)</b>
SiO <sub>2</sub>	400	80 ± 1.3	0.2 ± 0.1
	800	129 ± 2.3	11.8 ± 3.4
Al <sub>2</sub> O <sub>3</sub>	400	86 ± 2.5	0.5 ± 0.1
	800	134 ± 2.4	3.8 ± 0.2
Si <sub>3</sub> N <sub>4</sub>	400	88 ± 1.9	0.4 ± 0.1
	800	125 ± 2.4	8.3 ± 3.1



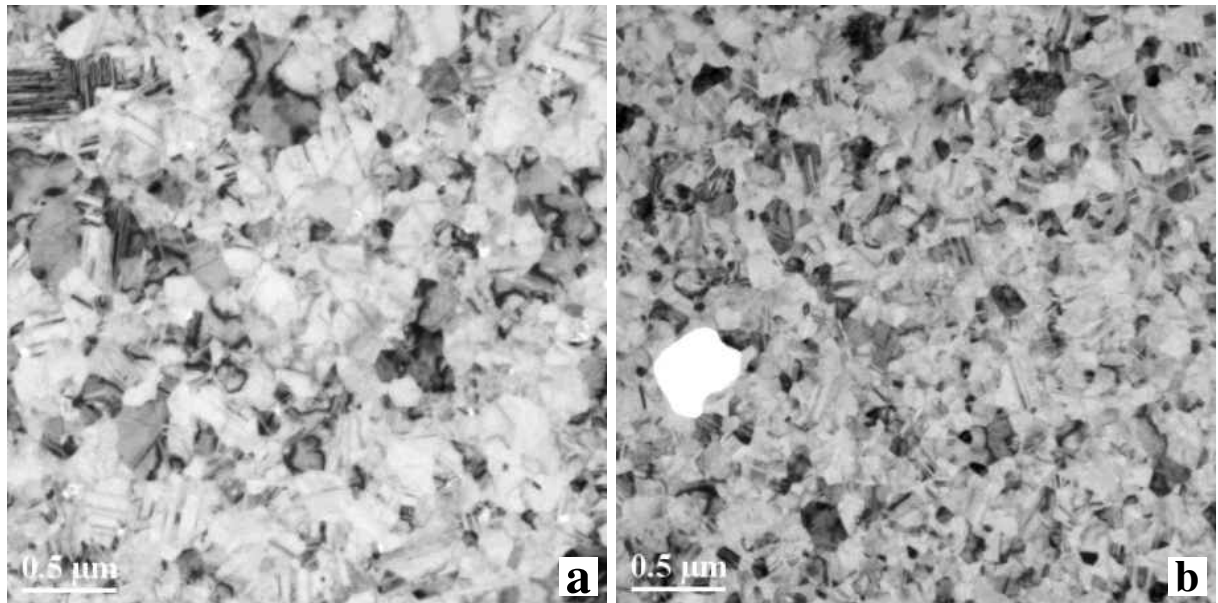


FIG. 5-6. Bright-field transmission electron micrograph of 40 nm Cu film encapsulated in 20 nm of  $\text{Al}_2\text{O}_3$  (a) annealed at 800 °C and (b) 1000 °C in  $\text{Ar}+3\%\text{H}_2$  for 40 minutes .

In addition to the annealing temperature, the effect of annealing time was also examined. FIG. 5-7 is a comparison of 40 nm Cu films encapsulated in  $\text{Al}_2\text{O}_3$  annealed at 800°C for 10 seconds (in rapid thermal annealing furnace), 40 minutes (in a tube furnace), and 160 minutes (in a tube furnace). It appears that the grain size is not a function of annealing time at this temperature but the longer annealing time does promote void formation.

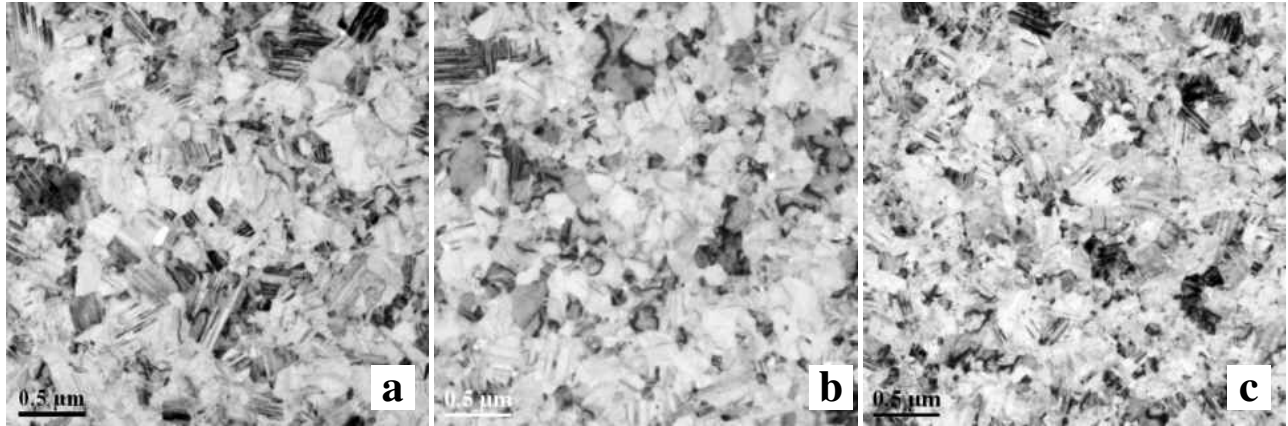


FIG. 5-7. Bright-field transmission electron micrograph of 40 nm Cu films encapsulated in 20 nm of  $\text{Al}_2\text{O}_3$  annealed at 800 °C for (a) 10 seconds (b) 40 minutes and (c) 160 minutes.

## 5.5 Conclusion

In this chapter, deposition parameters and post-deposition processing parameters to optimize grain growth and maintain microstructure stability in sub-50nm dielectric encapsulated thin films were examined. It was found that the  $\text{Ar}+\text{O}_2$  pre-deposition plasma etch, reduced substrate temperature during deposition, reduced deposition processing gas pressure, the use of dielectric amorphous encapsulation layer for the Cu film, the use of a reducing annealing gas, and annealing temperature all have positive effects in controlling grain size in the Cu layer in a dielectric encapsulated metal thin film structure. On the other hand, the use of RF bias to provide energetic particle bombardment and longer annealing times were found to be detrimental. The combination of these techniques allowed grain sizes larger than three times the Cu layer thickness in continuous films with minimal voiding. This control of grain size, in turn, enabled the independent variation of grain size and thickness that was the crucial

requirement for the successful experimental separation of grain size and film thickness effects on film resistivity, i.e., quantification of the classical size effect.

## CHAPTER 6

## RESISTIVITY SIZE EFFECT

### 6.1 Independent Variations

As discussed in previous chapters, the independent variation of film thickness and grain size is essential in measuring the relative contribution of the surface and grain boundary scattering quantitatively. In the last chapter, the methodology developed to control grain size in sub-50nm dielectric encapsulated Cu films is described. The primary samples for this work are sixteen  $\text{SiO}_2/\text{Cu}/\text{SiO}_2$  and six  $\text{SiO}_2/\text{Ta}/\text{Cu}/\text{Ta}/\text{SiO}_2$  samples with Cu layer thickness ranging from 27 nm to 158 nm and Cu grain size ranging from 35 nm to 425 nm that are used to study the relative contribution of grain boundary scattering to that of surface scattering in the classical size effect. The choice of Ta liners and  $\text{SiO}_2$  encapsulation layers are due, in part, to their wide usage in Cu interconnects for integrated circuits. The samples studied were relatively large grained samples, having an average grain size greater than the film thickness such that most grain boundaries are perpendicular to the film surfaces and few overlapping grain are present in plane-view TEM images. Further, the transparent  $\text{SiO}_2$  encapsulation layers provided better clarity for grain boundary identification. FIG. 6-1 shows the cross-sectional (on the left) and plan-view transmission electron micrograph images of a typical  $\text{SiO}_2/\text{Ta}/\text{Cu}/\text{Ta}/\text{SiO}_2$  samples. The film is continuous throughout, and the grain size is larger than film thickness such that only grain boundaries perpendicular to the film surface are present.

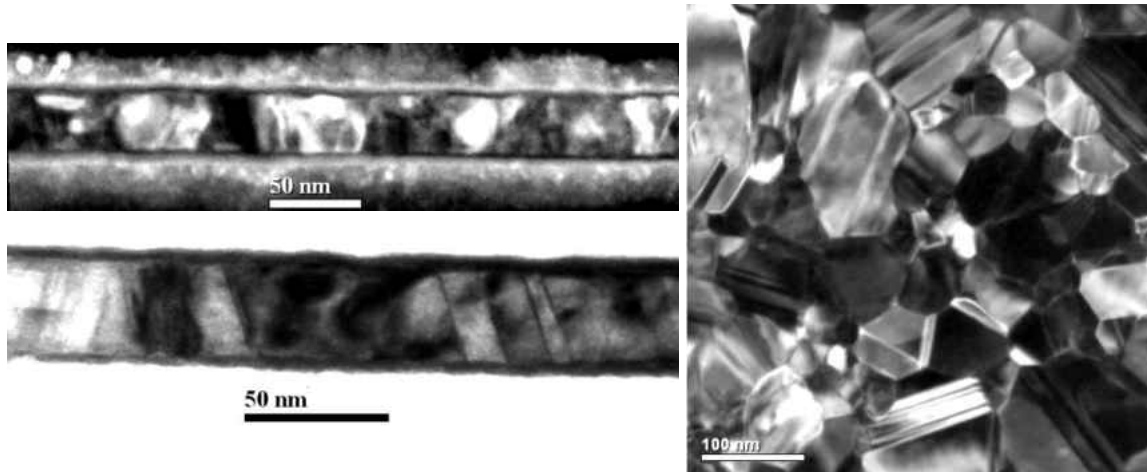


FIG. 6-1. Cross-sectional and HCDF plan-view transmission electron micrograph of 36.9 nm Cu film encapsulated in 20 nm of SiO<sub>2</sub> with 2nm of Ta liners annealed at 600 °C.

FIG. 6-2 is a plot of experimentally measured grain size versus Cu layer thickness (filled circles) to demonstrate that independent variation (with grain size from  $\sim 1.2x \sim 3.1x$  of Cu layer thickness) was achieved amongst the 22 samples studied. Although a fully independent variation (exhibited by unfilled circles) was not achieved, the careful quantification of grain size exercised in this work (error less than  $\sim 7\%$ ) ensures that the degree of independent variation achieved was sufficient for the separate quantification of grain boundary and surface scattering effects.

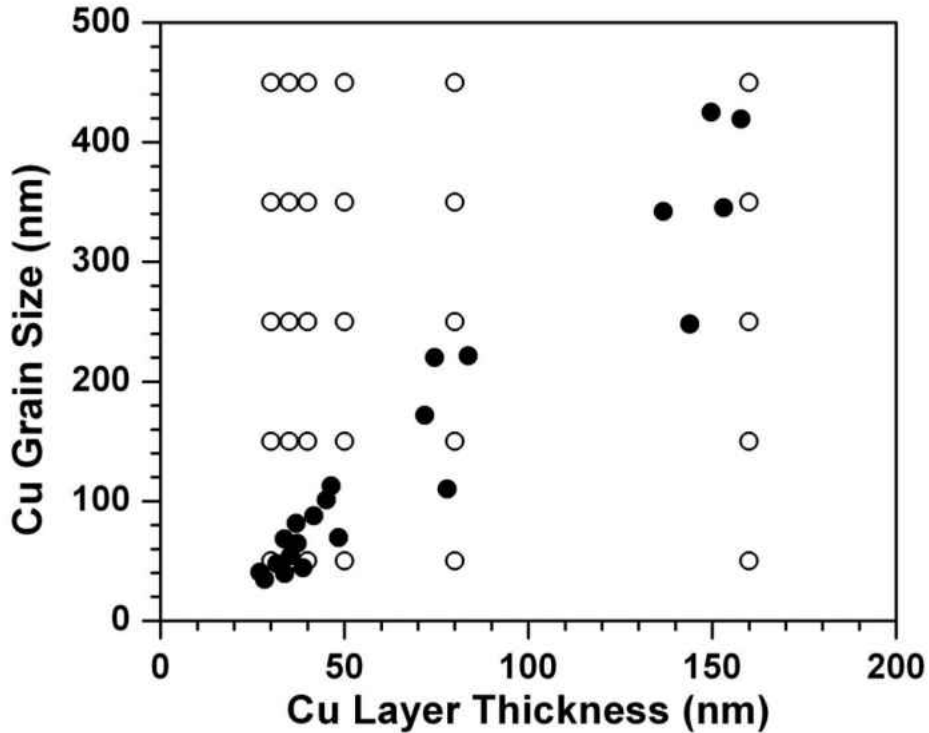


FIG. 6-2. Plot of grain sizes of Cu thin films as a function of Cu layer thickness for the sixteen  $\text{SiO}_2/\text{Cu}/\text{SiO}_2$  and six  $\text{SiO}_2/\text{Ta}/\text{Cu}/\text{Ta}/\text{SiO}_2$  samples studied in this work. The open circles show an example of an ideal data set, without correlation between the two variables, and the filled circles are the experimental data from Table 1.

## 6.2 Resistivity Size Effect at Room Temperature

In FIG. 6-3 (a), the resistivities of the  $\text{SiO}_2/\text{Cu}/\text{SiO}_2$  and  $\text{SiO}_2/\text{Ta}/\text{Cu}/\text{Ta}/\text{SiO}_2$  samples are plotted as a function of thickness at room temperature (RT), typically 296 K in the laboratory. The FS model (using equation 1a) is shown by the lines in the figure and fails to describe the experiment even with the most extreme value for the specularity coefficient ( $p = 0$ ) allowed by the

model. Within the  $\text{SiO}_2/\text{Cu}/\text{SiO}_2$  samples, it can be seen that for samples of similar thickness the resistivity decreases with increasing annealing temperature. Further, the Cu samples with Ta liners are found to have consistently higher resistivities than those without Ta. The presence of samples with different resistivities at each thickness indicates that surface scattering alone can not explain the resistivity size effect in these Cu thin films.

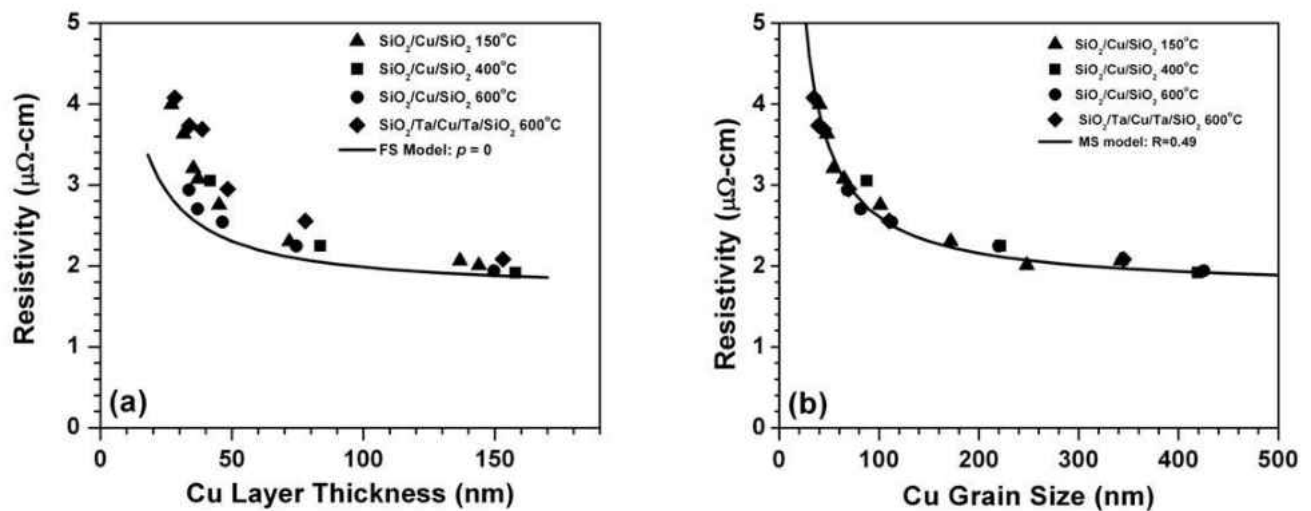


FIG. 6-3. The room temperature resistivity of  $\text{SiO}_2/\text{Cu}/\text{SiO}_2$  and  $\text{SiO}_2/\text{Ta}/\text{Cu}/\text{Ta}/\text{SiO}_2$  thin films a) as a function of Cu layer thickness,  $h$ , and b) as a function of Cu layer grain size,  $g$ . The data points correspond to the samples listed in Table 1. The solid curve corresponds to the FS model (equation 1a) in (a) and MS (equation 4a) model in (b).

FIG. 6-3 (b) is a plot of the same room resistivity values, now as a function of grain size. The experimental data points are clearly more tightly clustered about a single arc, and curve shown (the predictions of the MS model using equation 4a) provides a better fit with a reflection

coefficient of  $R = 0.49$ ) to the measured resistivity of the samples than that of the FS model with no other variable parameters. Further, the variations in resistivity associated with the annealing temperature or the presence of Ta are no longer present, but are instead accounted for by sample grain size. These results suggest that grain boundary scattering is the dominant mechanisms for classical size effect in our samples.

To further quantify our observations, the data from Table 1 is compared to the models previously described in Chapter 2. The sum of the residual squared error (SSE),  $\sum(\rho_{\text{exp}} - \rho_{\text{model}})^2$ , where differences between the calculated resistivity from a model are subtracted from the experimentally measured resistivity and squared, and where the summation is then taken over the twenty two room temperature experimental resistivity values in Table 1, is used as a measure of the model's ability to describe the experiment. Table 3 lists the parameters used in fitting the models to the experimental data, the optimum values of those parameters found within the physical limits allowed by each model (e.g.,  $0 < p < 1$ ), and the SSE for each of the following models: the Soffer model (equation 2), the FS model (equation 1a), the MS model (equation 4a), the Soffer+MS model (equation 6b), the MSS model (equation 5), the FS+MS model (equation 6a), the FS+MS model with "Caps", and the RK+MS model (equation 6c). In the fitting of FS+MS models, two different assumptions regarding the surface scattering were considered. In one case, identical scattering from the Cu/SiO<sub>2</sub> and the Cu/Ta interfaces was presumed and a single specularly parameter was used for the combined data. In the second case, two separate specularly parameters were used for the Cu/SiO<sub>2</sub> and for the Cu/Ta interfaces and this model variation is identified as "Caps" (equation 6a but with different specularly coefficients



for Cu/SiO<sub>2</sub> and Cu/Ta/SiO<sub>2</sub> interfaces). A fixed bulk resistivity value of 1.7 μΩcm due to phonon scattering is used (which corresponds to the 296 K room temperature of our laboratory) and a corresponding electron mean free path of 39 nm is also used for all models. As noted in Chapter 2, these ρ<sub>i</sub> values are those experimentally determined from high purity bulk Cu<sup>28</sup> and are not a varied fitting parameter. To further compare models having a similar minimum residual squared error, the F-test<sup>59</sup> (confidence level of 95%) was used to determine if an apparent improvement in fit (evidenced by a lower SSE) was statistically significant.

Table 3. A summary of classical modes, model fitting SSE's, and model fitting parameters.

<b>Room Temperature Resistivity Fittings</b>		
<b>Model Name</b>	<b>Sum Square Error (μ<sup>2</sup>Ω<sup>2</sup>cm<sup>2</sup>)</b>	<b>Model Parameters</b>
<b>Soffer</b>	<b>9.0</b>	<b>n/a</b>
<b>FS</b>	<b>8.9</b>	<b><i>p</i> = 0</b>
<b>MS</b>	<b>0.32</b>	<b><i>R</i> = 0.49</b>
<b>Soffer+MS</b>	<b>0.39</b>	<b><i>R</i> = 0.31</b>
<b>FS+MS</b>	<b>0.23</b>	<b><i>p</i> = 0.52 <i>R</i> = 0.43</b>
<b>MSS</b>	<b>0.23</b>	<b><i>p</i> = 0.55 <i>R</i> = 0.43</b>

The residual error from fitting experimental data to any physical model is not only a result of experimental error, but it is also the result of the limitations of the physical model. The large summed squared error of 8.9 μ<sup>2</sup>Ω<sup>2</sup>cm<sup>2</sup> observed with the FS model when fitting the room temperature resistivity as a function of thickness indicates that it clearly fails to describe the

experiment, even with the most extreme value allowed for the specular coefficient ( $p = 0$ ). Similarly, the Soffer model for surface scattering fails to describe the data, having a larger summed squared error of  $9 \mu\Omega^2\text{cm}^2$ . As is also seen in FIG. 6-3, the MS grain boundary scattering model (figure FIG. 6-3 (b)) is a dramatic improvement over the FS surface scattering model (FIG. 6-3 (a)). A much reduced summed squared error of  $0.32 \mu\Omega^2\text{cm}^2$  is obtained when fitting the room temperature resistivity data as a function of grain size to that of the MS model, and this result is statistically significant at a 99% confidence.

More complex models can be used to further reduce the residual error; however, the statistical significance of the reduced error must be considered before conclusions regarding the physical meaning of the improvement are made. This was done in drawing the following conclusions. The FS+MS model (using a simple Matthiessen's rule addition of surface and grain boundary scattering effects) with a summed squared error of  $0.23 \mu\Omega^2\text{cm}^2$  provides an improved fit over the MS model. However, this improvement is not statistically significant. Consequently, the presence of a surface scattering mechanism is not confirmed by this data.

The role of interfacial roughness was further explored by comparing our data to the Soffer+MS model. This model provides slightly higher SSE ( $0.37 \mu^2\Omega^2\text{cm}^2$ ) than that of the MS model by itself ( $0.32 \mu^2\Omega^2\text{cm}^2$ ). This is understood as the Soffer model can only provide a result equivalent to a fully diffusive scattering interface (in terms of the FS model) for surfaces having roughness in the range of 0.1 nm to 5 nm. Accordingly, the model can not distinguish the room temperature resistivity effect due to roughness variations in our samples, which range from 0.2 nm to 2 nm. From this, we conclude that the Soffer model fails to correctly describe the physics of the resistivity size effect at room temperature.

When fitting the MSS model to the RT resistivity data, the optimized specular and reflection coefficients are similar to the FS+MS, as the interaction effect between grain boundary and surface scattering is not significant at room temperature due to phonon scattering (see FIG. 2-2 above). For room temperature data, these two models are not distinguishable.

### 6.3 Resistivity Size Effect at 4.2 K

In interpreting the resistivity size effect at 4.2 K, the choice of electron mean free path value is crucial. As mentioned in Chapter 2, the relationship:  $\rho_1 \lambda = 6.6 \times 10^{-14} \Omega \text{m}^2$ <sup>15,22</sup> holds in bulk single crystal Cu samples for all temperatures. Mayadas and Shatzkes suggested that mean free path value should be of the order of the grain size when interpreting resistivity size effects in a polycrystalline material below room temperature, since they believed that the electrons will be scattered by the grain boundaries in a manner similar to that by phonons, so the electron mean free path can not become nearly infinitely long at temperatures near 0 K.<sup>15</sup> In contrast, the FS model would neglect the grain boundaries and use the long, single crystal value of the electron mean free path at low temperature. We have found that the MS approach overestimates the resistivity size effects at 4.2 K for the samples. Rather, it is found that a fairly long mean free path of 33  $\mu\text{m}$ , calculated using the above single crystal relationship, best describes the 4.2 K experimental resistivity data for all of the models using optimized parameters of the models having values similar to those found in the RT analysis. This issue will be examined again later, when modeling both the RT and 4.2 K data with a single set of optimized parameters.

In figure FIG. 6-4 (a), the 4.2 K resistivities of the  $\text{SiO}_2/\text{Cu}/\text{SiO}_2$  and  $\text{SiO}_2/\text{Ta}/\text{Cu}/\text{Ta}/\text{SiO}_2$  samples are plotted as a function of thickness. The FS model (using equation 1a) is shown by the

lines in the figure and, again, fails to describe the 4K resistivity values with fully diffusive scattering ( $p = 0$ ). Similar trends to the room temperature resistivity data can be seen in the 4.2 K resistivity data. Samples with higher annealing temperature resulting in lower resistivities, and samples with Ta liners are found to have high resistivity compared to their  $\text{SiO}_2/\text{Cu}/\text{SiO}_2$  counterparts.

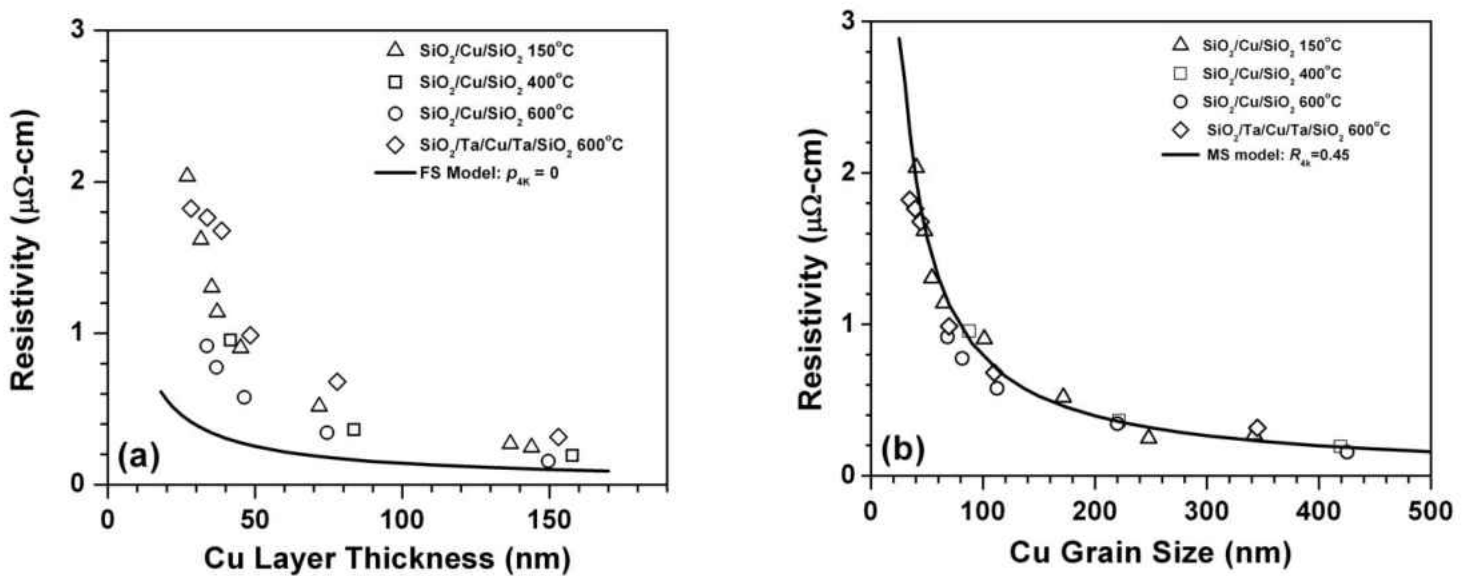


FIG. 6-4. The 4.2 K resistivity of  $\text{SiO}_2/\text{Cu}/\text{SiO}_2$  and  $\text{SiO}_2/\text{Ta}/\text{Cu}/\text{Ta}/\text{SiO}_2$  thin films a) as a function of Cu layer thickness,  $h$ , and b) as a function of Cu layer grain size,  $g$ . The data points correspond to the samples listed in Table 1. The solid curve corresponds to the FS model (equation 1a) in (a) and MS (equation 4a) model in (b).

FIG. 6-4 (b) is a plot of the low temperature resistivity as a function of grain size. Similar to the case of room temperature resistivity, variations in resistivity associated with the

annealing temperature or the presence of Ta are no longer present, but are instead accounted for by sample grain size. It is obvious that the MS model fits the resistivity data more readily than the FS model, with an optimized MS reflection coefficient value of  $R = 0.45$ . However, this 4.2 K reflection coefficient is slightly lower than the RT reflection coefficient at  $R = 0.45$ . According to the MS model, the reflection coefficient is expected to be constant at all temperatures, as the strength of the barrier potential of the grain boundary was assumed to be temperature independent.<sup>15</sup> The presence of two distinct reflection coefficients suggests either that the barrier potential of the grain boundary is different between RT and 4.2 K or that there are other temperature dependent scattering mechanisms at play.

To quantify the limits of our experimental data in understanding the resistivity size effect, the data at 4.2 K are compared to various models in a similar manner as the RT data was analyzed. Table 4 lists the parameters used in fitting the models to the 4.2 K data, the optimum values of those parameters found within the physical limits allowed by each model, e.g.,  $0 < p < 1$ , and the SSE for each the following models: the Soffer model (equation 2), the FS model (equation 1a), the MS model (equation 4a), the Soffer+MS model (equation 6b), the MSS model (equation 5). At 4.2 K, a fixed resistivity of  $0.002 \mu\Omega\text{cm}$  and an electron mean free path of  $33 \mu\text{m}$  were used.<sup>28</sup> Table 4 lists the parameters used in fitting the models to the 4.2 K data, the optimum values of those parameters found within the physical limits allowed by each model, e.g.,  $0 < p < 1$ , and the SSE for each the following models: the Soffer model (equation 2), the FS model (equation 1a), the MS model (equation 4a), the Soffer+MS model (equation 6b), the MSS model (equation 5). At 4.2 K, a fixed resistivity of  $0.002 \mu\Omega\text{cm}$  and an electron mean free path of  $33 \mu\text{m}$  were used.<sup>28</sup>

Table 4. A summary of classical models, model fitting SSE's, and model fitting parameters for samples measured at 4.2 K. .

<b>4.2 K Resistivity Fittings</b>		
<b>Model Name</b>	<b>Sum Square Error (<math>\mu^2\Omega^2\text{cm}^2</math>)</b>	<b>Model Parameters</b>
<b>Soffer</b>	<b>21.5</b>	<b>n/a</b>
<b>FS</b>	<b>14.0</b>	<b><math>p = 0</math></b>
<b>MS</b>	<b>0.27</b>	<b><math>R = 0.45</math></b>
<b>Soffer+MS</b>	<b>0.24</b>	<b><math>R = 0.43</math></b>
<b>FS+MS</b>	<b>0.25</b>	<b><math>p = 0.55</math> <math>R = 0.43</math></b>
<b>MSS</b>	<b>0.25</b>	<b><math>p = 0.77</math> <math>R = 0.42</math></b>

Similar to the case of fitting the RT experimental data, the resistivity increase as a function of thickness predicted by the 4.2 K FS and Soffer models are much lower than the experimentally measured 4.2 K resistivity, and large summed squared errors of  $14 \mu^2\Omega^2\text{cm}^2$  and  $21.5\mu^2\Omega^2\text{cm}^2$  are observed, respectively. Notice that the SSE for the FS and Soffer models is larger at 4.2 K than at room temperature. The greater SSE is due to the fact that the FS and Soffer models predict a significantly lower surface scattering at low temperature and the size effect resistivity of our samples changes little between room temperature and 4.2 K. The 4.2 K MS grain boundary scattering model is a better fit to the experimental resistivity data than the FS surface scattering model at a 99% confidence level.

As for the combined models, the FS+MS model shows improvement over the MS model, but the improvement is, again, not statistically significant and does not provide confirmation of a surface scattering contribution. The similarity between the specularity and reflection coefficients

of the 4.2 K and RT data is consistent to what is predicted by the FS and MS theory, as neither the Fermi potential at the interface nor that at the grain boundary is a function of temperature. Surprisingly, the Soffer+MS model ( $SSE = 0.24\mu^2\Omega^2\text{cm}^2$ ) provides better fit to the 4.2 K resistivity data than the FS+MS model ( $SSE = 0.25\mu^2\Omega^2\text{cm}^2$ ), unlike the RT data fitting. At the range of 0.1 nm to 0.2 nm, the Soffer model is sensitive to roughness variations, despite being indifferent at RT. This exposes the inherent failure of Soffer model, since the interaction of electrons with a rough surface is only a function of average electron wavelength, which is temperature independent.

The MSS model expects an additional resistivity contribution from the interaction between surface and grain boundary scattering at 4.2 K. Thus, the specular and reflection coefficient of the MSS model are slightly smaller than that of the FS+MS model to accommodate the additional resistivity due to interactions described by the model.

## 6.4 Summary

In this chapter, the classical size effect of sixteen  $\text{SiO}_2/\text{Cu}/\text{SiO}_2$  and six  $\text{SiO}_2/\text{Ta}/\text{Cu}/\text{Ta}/\text{SiO}_2$  samples has been investigated at RT and 4.2 K separately. The samples demonstrate an adequate level of independent variation of thickness and grain size. It is found that grain boundary scattering MS model provides a better description of the data set than the surface scattering FS model. This finding indicates grain boundary scattering is the dominant mechanism for resistivity size effect in this set of samples. Combined FS+MS and MSS models may also present valid descriptions of sample resistivity, but their statistical significance over the MS model was not been established. In other words, this analysis indicates that there is a possibility that surface and grain boundary scattering coexist in our samples, but grain boundary

scattering dominates.



## CHAPTER 7                      TEMPERATURE DEPENDENCE OF THE CLASSICAL SIZE EFFECT

In last chapter, it was found that MS model provided a better description of the classical size effect at both RT and 4.2 K. It was observed that different grain boundary reflection coefficients were found by optimization (reduction of SSE) at each temperature. To further understand the difference between the experimental resistivity data and these models, the resistivity increase (above bulk resistivity value) due to classical effect at both room temperature and 4.2 K is plotted as a function of grain size in FIG. 7-1. The filled symbols are resistivity increase measured at RT ( $\Delta\rho^{\text{RT}}$ ), and the open symbols are resistivity increase measured at 4.2 K ( $\Delta\rho^{4.2\text{K}}$ ). The solid curve corresponds to the resistivity increase predicted by MS grain boundary scattering ( $\Delta\rho_{\text{MS}}$ ) with only one optimized reflection coefficient of  $R = 0.47$ . A few trends can be observed in FIG. 7-1.  $\Delta\rho^{\text{RT}}$  is pair-wise higher than  $\Delta\rho^{4.2\text{K}}$  for all of the 22 samples, averaging  $\sim 10\%$  higher which is significantly less than the  $>60\%$  resistivity increase predicted by the FS or Soffer models over this temperature range. The experimental temperature dependence confirms the early observation that surface scattering is not the dominant scattering mechanism in the samples. However, as the experimental resistivities at room temperature are generally higher than the 4.2K values, and the MS model optimized for the combined data set is intermediate, further analysis is needed.

This temperature dependence may reflect limitations inherent in the MS model (e.g., the potential barrier of the grain boundary is temperature dependent, or there is diffuse scattering from parallel grain boundaries) or this may indicate the presence of a surface scattering

contribution to the resistivity, such as that given by the FS model, which has significant temperature dependence (FIG. 2-4).

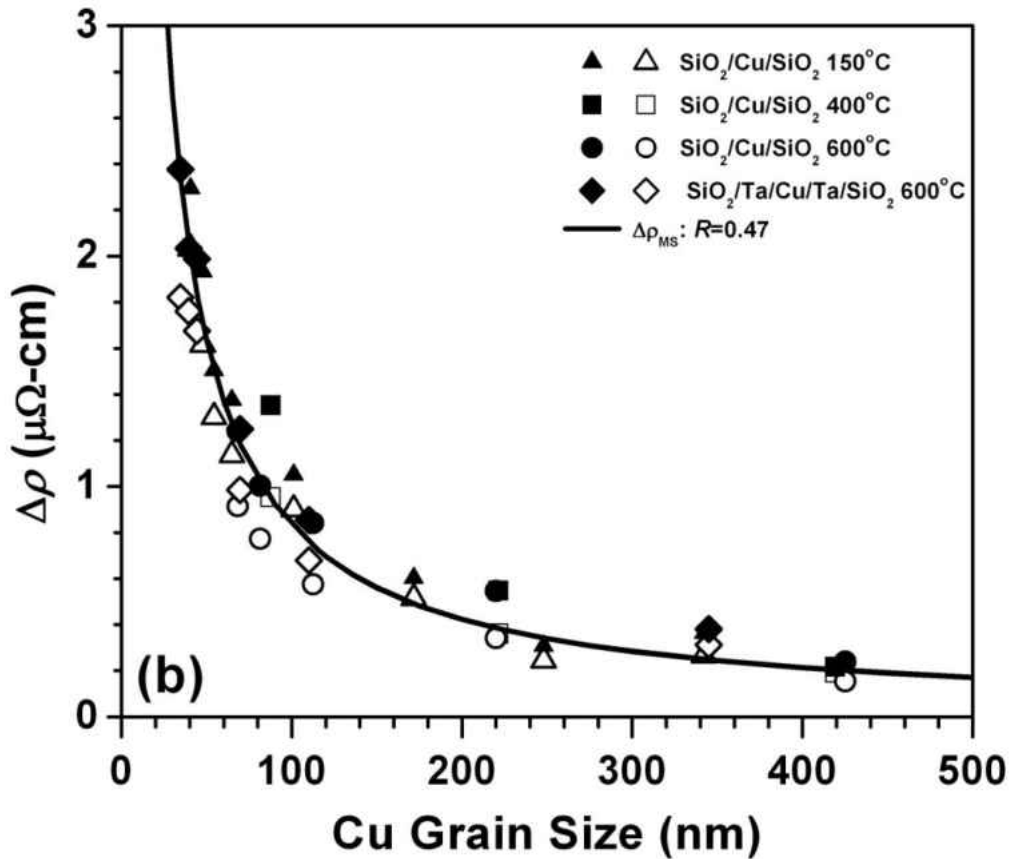


FIG. 7-1. The resistivity increase of  $\text{SiO}_2/\text{Cu}/\text{SiO}_2$  and  $\text{SiO}_2/\text{Ta}/\text{Cu}/\text{Ta}/\text{SiO}_2$  thin films due to size effect ( $\Delta\rho$ ) plotted as a function of Cu layer grain size,  $g$ . The filled symbols are resistivities measured at room temperature, and the open symbols are resistivities measured at 4.2 K. The data points correspond to the samples listed in Table 1. The solid curve corresponds to the resistivity size effect due to MS grain boundary scattering ( $\Delta\rho_{\text{MS}}$ ).

To analyze the temperature behaviors of various scattering mechanisms, both the 4.2 K and RT experimental data are compared against various models with one set of optimized parameters over both temperatures as shown in Table 5. Table 5 lists the parameters used in fitting the models to the experimental data, the optimum values of those parameters found within the physical limits allowed by each model, e.g.,  $0 < p < 1$ , and the sum of the squared residual error for each these models: the Soffer model (equation 2), the FS model (equation 1a), the MS model (equation 4a), the Soffer+MS model (equation 6b), the MSS model (equation 5), the MST model (equation 4a with separate reflection coefficients at room temperature and 4.2 K), the FS+MS model (equation 6a), the FS+MS model with “Caps” and the RK+MS model (equation 6c). In the fitting of FS+MS models, two different assumptions regarding the surface scattering were considered. In one case, identical scattering from the Cu/SiO<sub>2</sub> and the Cu/Ta interfaces was presumed and a single specular parameter was used for the combined data. In the second case, two separate specular parameters were used for the Cu/SiO<sub>2</sub> and for the Cu/Ta interfaces and this model variation is identified as “Caps.” At RT, a fixed bulk resistivity value of 1.7  $\mu\Omega\text{cm}$  and an electron mean free path of 39 nm were used for all models. At 4.2 K, a fixed resistivity of 0.002  $\mu\Omega\text{cm}$  and an electron mean free path of 33  $\mu\text{m}$  were used.

Table 5. A summary of classical models, model fitting SSE's, and model fitting parameters for data at RT and 4.2 K.

<b>Model Name</b>	<b>Sum Square Error (<math>\mu\Omega^2\text{cm}^2</math>)</b>	<b>Model Parameters</b>
Soffer	30.5	none
FS	22.9	$p = 0$
MS	0.96	$R = 0.47$
Soffer+MS	2.39	$R = 0.38$
MSS	0.85	$p = 0.61$ $R = 0.42$
MST	0.59	$R_{RT} = 0.49$ $R_{4.2K} = 0.45$
FS+MS	0.48	$p = 0.52$ $R = 0.43$
FS+MS (Caps)	0.48	$p_{\text{SiO}_2} = 0.51$ $p_{\text{Ta}} = 0.55$ $R = 0.43$
RK+MS	0.43	$p = 0.68$ $R = 0.43$ $n = 18.2$

The residual error from fitting experimental data to any physical model is not only a result of experimental error, but it is also the result of the limitations of the physical model. Again, the large SSE of  $22.9 \mu\Omega^2\text{cm}^2$  observed with the FS model when fitting our experimental data

indicates that it clearly fails to describe the experiment, even with the most extreme value allowed for the specular coefficient ( $p = 0$ ). The SSE of FS for fitting both RT and 4.2 K resistivities are just a simple sum of their respective SSE at each temperature. No additional source of errors have been introduced for fitting both RT and 4.2 K data at the same. Similarly, the Soffer model for surface scattering fails to describe the data, having a larger SSE of  $30.5 \mu^2\Omega^2\text{cm}^2$  which is also the sum of its SSE at each temperature.

The MS grain boundary scattering model is a dramatic improvement over the FS surface scattering model. However, a considerable summed squared error of  $0.96 \mu^2\Omega^2\text{cm}^2$  results, which is larger than the sum of SSE of fitting resistivities to MS model at RT ( $0.32\mu^2\Omega^2\text{cm}^2$ ) and 4.2 K ( $0.27\mu^2\Omega^2\text{cm}^2$ ) separately. The additional source of error come from the inability of the MS model to fit both the RT and 4.2 K resistivity increase with only one reflection coefficient as shown in FIG. 7-1.

The MST model (summed squared error of  $0.59 \mu\Omega^2\text{cm}^2$ ) allows the temperature dependence of the resistivity data to be better fitted by using separate (thus temperature dependent) grain boundary reflection coefficients at 4.2 K and at RT. This does provide a significantly better fit of the data than the MS model, and confirms that the MS model alone does not provide the correct temperature dependence. However, there are other physical models that also give the correct temperature dependence that require consideration. The FS+MS model (using a simple Matthiessen's rule addition of surface and grain boundary scattering effects) with a summed squared error of  $0.48 \mu\Omega^2\text{cm}^2$  provides a significantly improved fit over both the MS and MST models. Based on this improved fit, we conclude that thickness dependence is present in the experimental data at a statistical confidence level of 99%. Given this thickness dependence, there

is no need to invoke additional temperature dependence to the MS model with the MST model. The presence of both a temperature dependence and a residual thickness dependence in our experimental data confirms the presence of a weak surface scattering contribution (over and above that from grain boundary scattering) to the size effect in Cu.

Table 5 gives the grain boundary scattering reflection coefficient of 0.43 and surface scattering specularity coefficient of 0.52 for the combined FS+MS model. This intermediate value for the specularity coefficient is in contrast to the many previous works, wherein a surface specularity coefficient of zero was assumed, which simply maximized the surface scattering contribution to the resistivity increase.<sup>22,30</sup> For our samples, the partition into surface and grain boundary contributions to the resistivity size effect provides averages of 27% from surface scattering and 73% from grain boundary scattering for room temperature. At 4.2 K, the contribution from surface scattering is 14%, while that from grain boundary scattering is 86%.

More complex models can be used to further reduce the residual error; however, the statistical significance of the reduced error must be considered before conclusions regarding the physical meaning of the improvement are made. This was done in drawing the following conclusions. To further explore the role of the interface properties on surface scattering, the FS+MS model was extended (FS+MS(Caps)) to include different specularity coefficients for the

two interfaces studied ( $p_{\text{SiO}_2}$  and  $p_{\text{Ta}}$ , for Cu/SiO<sub>2</sub> and Cu/Ta interfaces, respectively). Surprisingly, this did not improve the residual summed squared error, nor did it change the grain boundary reflection coefficient from 0.43  $\mu\Omega^2\text{cm}^2$ . This confirms that, in spite of the higher resistivities observed for the SiO<sub>2</sub>/Ta/Cu/Ta/SiO<sub>2</sub> samples, little of the resistivity increase can be attributed to differences in the surface scattering of conduction electrons at the Cu/Ta and Cu/SiO<sub>2</sub> interfaces. Rather the resistivity increase is a simple consequence of the smaller grain size present in the SiO<sub>2</sub>/Ta/Cu/Ta/SiO<sub>2</sub> samples (Table 1).

The role of interfacial roughness was further explored by comparing our data to the Soffer+MS and RK+MS models. The Soffer+MS model actually provides a worse fit (2.39  $\mu\Omega^2\text{cm}^2$ ) than the MS model by itself (0.96  $\mu\Omega^2\text{cm}^2$ ) due, in part, to its temperature dependence. From this, we conclude that the Soffer model fails to correctly describe the physics of the resistivity size effect. However, the RK model does reduce the summed squared residual error from that of the FS+MS (0.48  $\mu\Omega^2\text{cm}^2$ ) to 0.43  $\mu\Omega^2\text{cm}^2$ . This fitting was performed with the thickness parameter,  $n$ , of 18.2 nm, where  $n$  was determined by minimization of the residual error instead of by a Monte-Carlo simulation. While this reduction in error justifies additional efforts to relate surface roughness to resistivity, it is worth noting that the improvement observed was not statistically significant.

The MSS model differs from the FS+MS model in that it includes the interaction between grain boundary and surface scattering. The optimum parameters for the MSS model to describe our data are  $p = 0.61$  and  $R = 0.42$ . However, with a summed squared error of 0.85  $\mu\Omega^2\text{cm}^2$ , the MSS model is a significantly worse description of our data than the FS+MS model, primarily as it overestimates resistivities at low temperature (as shown in figure 2). Thus, we conclude that the

interaction of surface and grain boundary scattering postulated by Mayadas and Shatzkes and expected to be evident at low temperatures (in the absence of phonon scattering) does not occur. The observed absence of increased surface scattering due to the presence of grain boundaries (a lack of interaction) indicates that while the grain boundary scattering in our samples necessarily changes the in-film-plane component of electron momentum, it does not significantly increase the out-of-film-plane component, normal to the external surfaces. This means that electrons that are in initial states having momentum parallel to the external surfaces are scattered into final states having momentum parallel to the external surfaces, or, in other words, if the electron was not travelling toward the surface when it encountered the grain boundary, it will not be sent toward the surface after scattering from the grain boundary as shown in FIG. 7-2. By contrast, Mayadas and Shatzkes assumed that the electrons that scattered at the grain boundaries did so into all possible momentum states, similar to a “diffuse” surface scattering event. While we do not hypothesize that grain boundary scattering is “specular,” it does appear that the components of electron momentum that are parallel to the grain boundary planes are conserved. Note that this is very different from the case of a diffuse scattering event at the conductor’s external surface which does not preserve the momentum components parallel to the surface (FIG. 2-3). This explains the observed simple summation of surface and grain boundary resistivities and suggests a fundamental difference between surface and grain boundary scattering.





FIG. 7-2. Schematic of the FS+MS combined model where no interaction occurs between grain boundary and surface at low temperature.

## CHAPTER 8

## SUMMARY, SIGNIFICANCE, AND FUTURE

### WORK

In this work, the contributions of surface scattering and grain boundary scattering to the resistivity increase observed with the reduction of conductor thickness in polycrystalline Cu thin films through quantitative measurement of the primary experimental variables and comparison of the data to accepted models has been carefully examined. The samples studied were relatively large grained samples, having independent variations of grain size and Cu layer thickness. It was found that grain boundary scattering was the dominant scattering mechanism and provided an unambiguous experimental verification of the grain boundary scattering model of Mayadas and Shatzkes. A measurement of the surface scattering for our samples finds the surface scattering effect in the samples are well described by the Fuchs-Sondheimer model with an intermediate value,  $p = 0.52$ , for the surface specularity coefficient. This value is in contrast to prior reports where fully diffuse scattering surfaces ( $p = 0$ ) were claimed. It was also found that the increase in surface scattering at low temperatures modeled by Mayadas and Shatzkes and resulting from grain boundary scattering was not evident. The surface scattering from Cu/SiO<sub>2</sub> and Cu/Ta interfaces was found to be indistinguishable. The data does suggest that there is a roughness dependence to the surface scattering, but this was not conclusively demonstrated. Voids and impurities were found to have negligible impact on the measured resistivities of the carefully prepared films.

Various processing procedures to optimize grain growth and maintain microstructure

stability in sub-50nm dielectric encapsulated thin films after annealing were also studied. It was found that the predeposition plasma etch, substrate temperature during deposition, deposition processing gas pressure, the use of dielectric amorphous encapsulation layer on Cu film, annealing gas, and annealing temperature all have positive effects in controlling grain size in the Cu layer in a dielectric encapsulated metal thin film structure. On the other hand, energetic particle bombardment and longer annealing time was found to matter little in helping achieving larger grains in our samples. The combination of such techniques has made producing grain size larger than three times the Cu layer thickness possible, while ensuring film continuity.

For applications of future generations of Cu interconnects, these results are significant. The physics of scattering at Cu/Ta interface and grain boundary are the same for both Cu interconnects and layered thin film samples used in this study. Therefore, the specular coefficients of 0.52 and reflection coefficient of 0.43 should be universal in all nano-scale Cu structures. Recently, Kitaoka et al. measured specular coefficient coefficient of 0.49 and reflection coefficient of 0.64 using STM four point probe over a 70nm wide Cu interconnect, which was comparable to our result. In fact, the only differences between Cu interconnect and our layered thin films in terms of the classical resistivity size effect are the additional side wall scattering and the higher concentration of impurities at the grain boundaries associated with the electroplating deposition process often used for Cu interconnects. The lack of interaction between grain boundary scattering and surface scattering suggests that these interactions may also be absent for narrow lines, where the scattering from surfaces that define the sides of the line (sidewalls) gives rise to an additional complication. If the sidewall scattering of lines is assumed

to be similar to that of the top and bottom surfaces of our films, and is an additive resistivity effect (no interaction), then grain boundary scattering is expected to be the dominant resistivity size effect for lines having equal height, width, and grain size. This is not unexpected, as all conduction electrons must cross grain boundaries to contribute to the current in the line whereas only some conduction electrons interact with the external surfaces. On the other hand, the higher impurity concentration found in Cu interconnect lines are expected to increase grain boundary scattering.<sup>22</sup> Our measured reflection coefficient of 0.43 serves as a lower bound; and the contribution of grain boundary scattering in Cu interconnects might be greater than that in thin films. The finding that surface scattering is largely independent of the chemistry of the external surface (Cu/SiO<sub>2</sub> and Cu/Ta providing similar results) is instrumental in designing next generation Cu liner deposition techniques in dual-damascene process. This suggests that practical efforts to reduce the resistivity of narrow interconnect lines should be directed towards processing changes to increase the conductor grain size rather than efforts to change the conductor external surface chemistry.

In the near future, a comparison of amorphous TaSiN as a barrier layer is underway, and larger grains have been observed in Cu thin film samples with TaSiN barrier layers. This might be part of a solution to reduced grain boundary scattering in future Cu interconnects. Studies of the resistivity increase of single grain boundaries of various structures and at various thickness at 4.2 K using a STM four point probe may also help to confirm our findings of the absence of interaction between surface and grain boundary scattering.

## **APPENDIX A RESISTANCE INCREASE DUE TO VOID FRACTIONS**

While resistivity models for highly voided (near percolation threshold) thin films can be found in the literature,<sup>60,61</sup> there is no published model suitable to describe the case of a low density of isolated voids, as we observe. This may be due to the relative simplicity of the calculation, which is presented below to show the small contribution of the voids to the resistivity increase observed in our work.

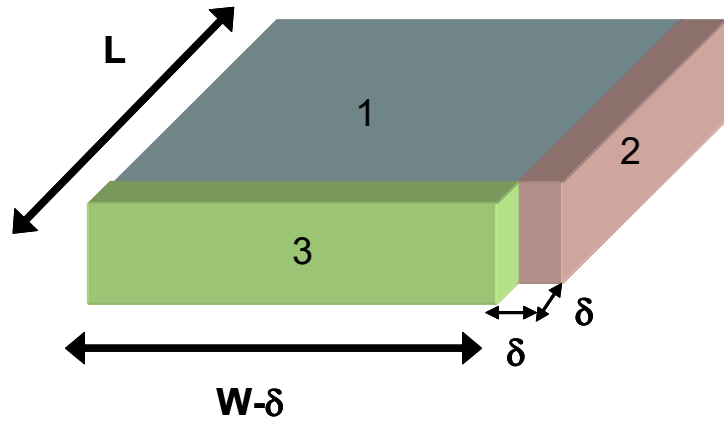
We can consider the resistance of a thin film of resistivity  $\rho$  to consist of many identical area elements, each of length,  $L$ , width,  $W$ , and thickness,  $h$ . The resistance,  $R_0$ , of each element is then just:

$$R_0 = \rho \frac{L}{W \times h},$$

where we have assumed the direction of current flow to be parallel to the dimension  $L$ . We can model the formation of voids in a film consisting of many such elements by adding a square hole (of equal width and length,  $\rho$ ) in one corner of each area element. This geometry is shown below for clarity. The additional scattering from the walls of the void are neglected as this is a small fraction of the total conductor surface area ( $\delta \ll L, W$ ). The voided area fraction is:

$$\% \text{ Voided Area} = \frac{\delta^2}{L \times W}$$

The resistance of the area element with the void can be calculated by considering the element to consist of two resistances in series. The first resistance is the region indicated by “3” in the



figure, which has a resistance,  $R_3$ , parallel to the  $L$  dimension, given by:

$$R_3 = \rho \frac{\delta}{(W - \delta) \times h_R}$$

Please note that in this equation  $h_R$  is the increased thickness of all three regions resulting from the redistribution of the Cu atoms. We will require the total volume of each area element to remain constant, independent of void area, to conserve the amount of Cu present in the film, and we will use this condition later to calculate  $h_R$ .

The second resistance in series consists of regions 1 and 2 combined,  $R_{1,2}$ , and this has a resistance parallel to the  $L$  dimension of:

$$R_{1,2} = \rho \frac{(L - \delta)}{W \times h_R}$$

The relative increase in resistance of each area element (and hence of the film) is given by

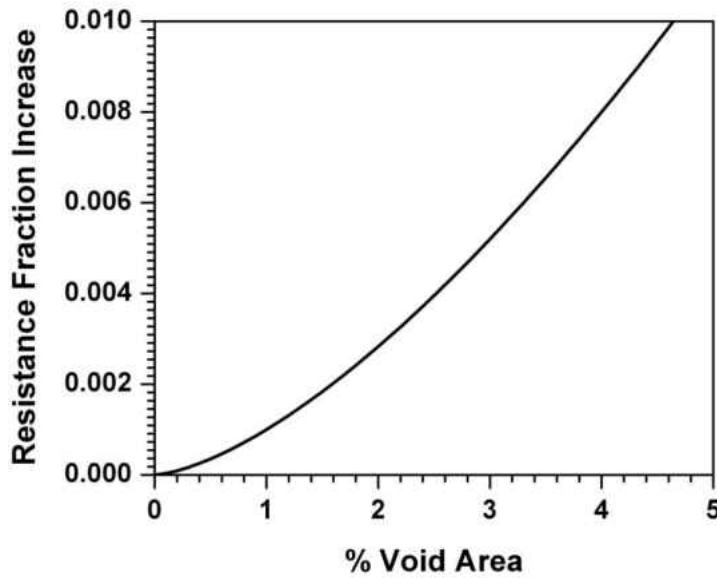
$$\% \text{ Resistivity Increase} = \frac{R_{1,2} + R_3 - R_0}{R_0},$$

from which  $h_R$  is determined by conserving the volume of our area element. The volume of the un-voided area element is just  $L \times W \times T$  and the volume of the area element with a void is given by  $[(L \times W) - \delta^2] \times h_R$ . Equating these gives:

$$\frac{h_R}{h} = \frac{L \times W}{(L \times W) - \delta^2}.$$

A plot of fraction of *Resistance Increase* as a function of *% Voided Area* calculated using the above equations is shown below.





These equations can be simplified further by taking  $L = W$  and by setting  $\frac{\delta}{L} = x$ . After algebraic manipulation this gives a very simple result,

$$\% \text{ Resistivity Increase} = x^3 .$$

As the  $\% \text{ Voided Area} = x^2$ , this gives the simple geometrical result:

$$\% \text{ Resistivity Increase} = (\% \text{ Voided Area})^{1.5}$$

This model is clearly limited to a low density of isolated (non-interacting) voids, and requires  $\delta \ll L$  in order for the current crowding near the edges of a void area to be neglected. For films with low void fractions (less than 5%) the resistivity error is less than 1% and negligible.

## APPENDIX B PUBLICATION LIST

1. **T. Sun**, Bo Yao, A. P. Warren, K. Barmak, M. F. Toney, R. E. Peale, and K. R. Coffey  
“Surface and grain boundary scattering in nanometric Cu films“, submitted for publication to  
Phys. Rev. B (2009)
2. **T. Sun**, A. P. Warren, B. Yao, K. Barmak, M. F. Toney, K. R. Coffey, “Quantitative analysis  
of the impact of surface and grain boundary scattering on the resistivity of nanometric Cu  
films”, accepted for publication in Advanced Metallization Conference proceedings (2009)
3. **T. Sun**, B. Yao, A.P. Warren, K. Barmak, M. F. Toney, R. E. Peale, and K. R. Coffey,  
“Dominant role of grain boundary scattering in the resistivity of nanometric Cu films”, Phys.  
Rev. B **79**, 041402 (2009)
4. **T. Sun**, B. Yao, V. Kumar, A.P. Warren, K. Barmak, and K. R. Coffey, “Classical Size Effect  
in Oxide-Encapsulated Cu Thin Films: Impact of Grain Boundaries versus Surfaces on  
Resistivity”, J. Vac. Sci. Technol. A **26**, 605 (2008)
5. **T. Sun**, B. Yao, V. Kumar, A.P. Warren, K. Barmak, and K. R. Coffey, “Resistivity Size Effect in  
Encapsulated Cu Thin Films”, in Proceedings of IITC., 141 (2008)
6. B. Yao, **T. Sun**, V. Kumar, K. Barmak, and K. R. Coffey, “ Grain growth and void formation

in dielectric encapsulated Cu thin films”, J. Mater. Res. **23**, 2033 (2008)

7. D.J. Shelton, **T. Sun**, J.C. Ginn, K.R. Coffey, G.D. Boreman, ”Relaxation time effects on dynamic conductivity of alloyed metallic thin films in the infrared band”, J. Appl. Phys. **104**, 103514 (2008).

## REFERENCES

---

- 1 J. J. Thomson, Proc. Cambridge Philos. Soc. **11**, 120 (1901).
- 2 F. Chen and D. Gardner, IEEE Electron Device Letters. **19**, 508 (1998).
- 3 “International technology Roadmap for Semiconductors, 2003 Edition, Executive Summary,” <http://public.itrs.net/>.
- 4 S. M. Rossnagel and T. S. Kuan, J. Vac. Sci. Technol. B **22**, 240 (2004).
- 5 P. Kapur and J. P. McVittie, IEEE Trans. Electron Devices **49**, 590 (2002).
- 6 V. Zhirnov, R. K. Cavin, D. J. C. Herr, and T. A. Wooldridge, IEEE Trans. IEEE Trans. Semicond. Manuf. **15**, 157 (2002).
- 7 P. Kapur, J. P. McVittie, and K. C. Saraswat, IEEE Int. Interconnect Tech. Conf. 233 (2001).
- 8 N. W. Ashcroft and N. D. Mermin, Solid State Physics (Saunders College, Philadelphia, 1976)
- 9 J.M. Ziman, Principles of the Theory of Solids (Cambridge University Press, 1969)
- 10 J.W.Lim and M. Isshiki, J. Appl Phys. **99**, 094909 (2006).
- 11 C.-U. Kim, J. Park, N. Michael, P. Gillespie, and R. Augur, J. Electron. Mater. **32**, 982 (2003).
- 12 R. Landauer, IBM J. Res. Dev., **1**, 223 (1957).
- 13 K. Fuchs, Proc. Cambridge Philos. Soc. **34**, 100 (1938).
- 14 E. H. Sondheimer, Adv. Phys. **1**, 1, (1952).
- 15 A. F. Mayadas and M. Shatzkes, Phys Rev. B **1**, 1382 (1970).

- 
- 16 D. Josell, C. Burkhard, Y. Li, Y.W. Cheng, R.R. Keller, C.A. Witt, D.R. Kelley, .E. Bonevich, B.C. Baker, and T.P. Moffat, *J. Appl. Phys.* **96**, 759 (2004).
- 17 J. R. Sambles, *Thin Solid Films* **106**, 321(1983).
- 18 G.Schindler, presentation for Sematech workshop on Cu resistivity (2005).
- 19 J. E. Parrott, *Proc. Phys. Soc.* **85** 1143 (1965).
- 20 J. M. Ziman, *Electrons and Phonons* (Oxford University Press, London, 1962), pp. 452-460.
- 21 S. G. Soffer, *J. Appl. Phys.* **38**, 1710 (1967).
- 22 W.Zhang, SH. Brongersma, Z. Li, D. Li, O. Richard, and K. Maex, *J. Appl. Phys.* **101**, 063703 (2007).
- 23 H.Marom and M. Eizenberg, *J. Appl. Phys.* **99**, 123705 (2007)
- 24 J.-W. Lim and M. Isshiki, *J. Appl. Phys.* **99**, 094909 (2006)
- 25 J. C. Hensel, R. T. Tung, J. M. Poate, and F. C. Unterwald, *Phys. Rev. Lett.* **54**, 1840 (1985).
- 26 R. C. Munoz, C. Arenas, G. Kremer, and L. Moraga, *J. Phys.: Condens. Matter* **15**, L177-L184 (2003) .
- 27 J. R. Sambles and K C Elsom, *J. Phys. D: Appl. Phys.* **15**, 1459 (1982).
- 28 D. R. Lide, in *CRC Handbook of Chemistry and Physics* 87th ed. (CRC-Press, Boca Raton, 2006), pp. 12-39.

- 
- 29 P.M. T. M. van Attekum, P. H. Woerlee, G. C. Verkade, and A. A. M. Hoeben, *Phys. Rev. B* **29**, 645 (1984)
- 30 H. Marom, J. Mullin, and M. Eizenberg, *Phys. Rev. B* **74**, 045411 (2006).
- 31 J. J. Plombon, E. Andideh, V. M. Dubin, and J. Maiz, *Appl. Phys. Lett.* **89**, 113124 (2006).
- 32 J. R. Sambles, K. C. Elsom, and D. J. Jarvis, *Phil. Trans. Roy. Soc. Lon. A.* **304**, 365 (1982).
- 33 JS Chawla and D Gall, *Appl. Phys. Lett.* **94**, 252101 (2009).
- 34 M. E. Day, M. Delfino, J. A. Fair, and W. Tsai, *Thin Solid Films* **254**, 285 (1995).
- 35 J. M. E. Harper, C. Cabral, Jr., P. C. Andricacos, L. Gignac, I. C. Noyan, K. P. Rodbell, and C. K. Hu, *J. Appl. Phys.* **86**, 2516 (1999).
- 36 H.-D. Liu, Y.-P. Zhao, G. Ramanath, S. P. Murarka, and G.-C. Wang, *Thin Solid Films* **384**, 151 (2001).
- 37 M. Avrekh, O. R. Monteiro, I. G. Brown, *Appl. Surf. Sci.* **158**, 217 (2000).
- 38 W. Steinhögl, G. Schindler, G. Steinlesberger, and M. Engelhardt, *Phys. Rev. B* **66**, 075414 (2002).
- 39 C. Durkan and M E. Welland, *Phys. Rev. B* **61** 14215 (2000).
- 40 A. Bietsch and B. Michel, *Appl. Phys. Lett.* **80** 3346 (2002).
- 41 Yusuke Kitaoka, Takeshi Tono, Shinya Yoshimoto, Toru Hirahara, \_ Shuji Hasegawa, and Takayuki Ohba, *Appl. Phys. Lett.* **95**, 052110 (2009).
- 42 L. Lu, Y. Shen, X. Chen, L. Qian, and K. Lu, *Science* **304** 422 (2004).
- 43 See <http://rsb.info.nih.gov/ij/>
- 44 D. T. Carpenter, J. M. Rickman, and K. Barmak, *J. Appl. Phys.* **84**, 5843 (1998).

- 
- 45 A. Gupta, A. Paul, S. Mukhopadhyay, *J. Appl. Phys.* **90**, 1237 (2001).
- 46 R. Schad, P. Belien, G. Verbanck, V. V. Moshchalkov, and Y. Bruynseraede, H. E. Fischer, S. Lefebvre, M. Bessiere. *Phys. Rev. B* **59**, 1242 (1999)
- 47 A. Ulyanenko, R. Matsuo, K. Omote, K. Inaba, and J. Harada, M. Ishino, M. Nishii, and O. Yoda, *J. Appl. Phys.* **87**, 7255 (2000).
- 48 J. M. Freitag, B. M. Clemens. *J. Appl. Phys.* **89**, 1101 (2001).
- 49 R. Schlattmann, J. D. Shindler, and J. Verhoeven. *Phys Rev. B* **54**, 10 880 (1996)
- 50 <http://www-ssl.slac.stanford.edu/beamlines/bl2-1/>
- 51 L. J. Van der Pauw, *Philips Res. Rep.* **13**, 1 (1958).
- 52 W. Wu, S. H. Brongersma, M. Van Hove, and K. Maex, *Appl. Phys. Lett.* **84**, 2838 (2004).
- 53 J. M. E. Harper and K. P. Rodbell, *J. Vac. Sci. Technol. B* **15**, 763 (1997).
- 54 J. L. Vossen and W. Kern, *Thin Film Processes II* (Academic, New York, 1991).
- 55 Ohring, M. *The Material Science of Thin Films* (Academic, San Diego, 1992).
- 56 . Nitta, T. Ohmi, M. Otsuki, T. Takewaki and T. Shibata. *J. Electrochem. Soc.* **139** (1992), p. 922.
- 57 R.A. Roy, J.J. Cuomo and D.S. Yee, *J. Vac. Sci. Technol. A* **6** 1621 (1986).
- 58 B. Yao, T. Sun, V. Kumar, K. Barmak, and K.R. Coffey, *J. Mater. Res.* **23**, 2033 (2008).
- 59 G. Casella and R.L. Berger, *Statistical Inference* (Duxbury, Pacific Grove, 2002), pp. 534.
- 60 C. Pennetta, L. Reggiani, and Gy. Trefán, *Phys. Rev. Lett.* **84**, 5006 (2000).
- 61 K. Sieradzki, K. Bailey, and T. L. Alford, *Appl. Phys. Lett.* **79**, 3401 (2001).